

Department of Technical Physics  
Faculty of Information Technology  
Helsinki University of Technology

# **DEVELOPMENT OF MULTICHANNEL SQUID MAGNETOMETERS FOR NEUROMAGNETIC MEASUREMENTS**

**Jukka Knuutila**

Thesis for the degree of Doctor of Technology to be presented  
with due permission for public examination and criticism in the  
Auditorium G at the Helsinki University of Technology, on the  
18th of December, 1987, at 12 o'clock noon.

Espoo 1987

ISBN 951-99903-6-4  
TKK Offset, Espoo 1987

# Contents

<b>Preface</b>	<b>1</b>
<b>1 Basic Concepts and Methods of Neuromagnetism</b>	<b>2</b>
1.1 Cellular Origin of the Electric and Magnetic Fields . . . . .	2
1.2 Modeling . . . . .	3
1.3 Data Analysis . . . . .	6
1.4 Spatial Resolution of MEG . . . . .	7
<b>2 Josephson Junctions</b>	<b>9</b>
2.1 Phase Coherence . . . . .	9
2.2 Electrical Characteristics of Josephson Junctions . . . . .	10
2.3 Fabrication of Thin-Film Tunnel Junctions . . . . .	12
<b>3 SQUID Magnetometers</b>	<b>16</b>
3.1 The rf SQUID . . . . .	16
3.2 The Autonomous dc SQUID . . . . .	17
3.2.1 Operation and Basic Characteristics . . . . .	17
3.2.2 White Noise and Energy Sensitivity . . . . .	20
3.2.3 Low Frequency Noise . . . . .	21
3.3 The Coupled dc SQUID . . . . .	22
3.3.1 Signal Coupling to the SQUID . . . . .	22
3.3.2 Effects of Flux-Coupling Circuits on SQUID Operation . . . . .	24
3.3.3 Optimization of the SQUID Magnetometer . . . . .	26
3.4 Signal Readout and Electronics for the dc SQUID . . . . .	27
<b>4 Multichannel Neuromagnetometers</b>	<b>29</b>
4.1 The State of the Art . . . . .	29
4.2 Design and Construction of Multichannel Magnetometers . . . . .	32
4.2.1 Design Criteria . . . . .	32
4.2.2 Planar Gradiometer Arrays . . . . .	33
4.2.3 Practical Aspects . . . . .	34
4.3 Use of Multichannel Magnetometers . . . . .	34
4.3.1 Calibration and Dewar Position Indication . . . . .	34
4.3.2 Correlated Noise . . . . .	35
4.3.3 Examples of MEG Measurements . . . . .	36

<b>5</b>	<b>Discussion</b>	<b>38</b>
5.1	New Superconductor Materials . . . . .	38
5.2	Clinical Applications . . . . .	39
5.3	Conclusions . . . . .	41
<b>6</b>	<b>Contents of the Thesis</b>	<b>42</b>
6.1	List of Publications . . . . .	42
6.2	Summary of Publications . . . . .	43
	<b>Acknowledgments</b>	<b>48</b>
	<b>References</b>	<b>50</b>

# Preface

In magnetoencephalography (MEG), magnetic fields generated by the brain are studied. Typical amplitudes of these fields are only 50 – 500 fT; thus, very sensitive magnetometers and good rejection of ambient noise are required. The superconducting quantum interference device, SQUID, is the only magnetic sensor of sufficient sensitivity for magnetoencephalographic experiments. The construction of SQUID magnetometers is the main topic of this thesis.

In a typical MEG experiment, the subject receives some sensory stimuli such as short tones. Several tens of milliseconds after the stimulation specific areas of the cerebral cortex are activated, and a rapidly changing magnetic field can be recorded. On the basis of the measured spatial field distribution of this evoked response it is possible to find the cortical area activated by the stimulus.

MEG locates sources of cortical activity with millimeter precision and with millisecond time resolution. It is possible to find the position of cortical sources not revealed by other noninvasive methods, e.g. electroencephalography (EEG). For a recent review on MEG, see Ref. [1].

So far, neuromagnetic measurements have been mostly carried out with single-SQUID instruments by repeating the recordings at several magnetometer locations. The use of only one channel severely limits the usefulness of the method: the measurements are slow, and the evoked responses may not stay stable because of the progressing fatigue of the subject. In addition, the study of non-repetitive phenomena, such as the spontaneous brain activity, requires simultaneous field measurements at several points.

At present, multi-SQUID systems have been or are being installed in several laboratories. In addition, the introduction of new SQUIDs with an improved sensitivity and the use of magnetically shielded rooms have enabled the construction of magnetometers in which the instrument noise is no longer the dominating noise source; the noise due to the subject has become the limiting factor of sensitivity.

The main aim of the work described in this thesis has been to design and build multichannel magnetometers for MEG measurements. Research and development work for obtaining low-noise dc SQUID sensors with smooth characteristics was a central part of this study; an integrated all-planar thin film sensor was one of the main goals.

In the introduction, an overview is given of the key concepts, methods, problems, and results in areas related to the work described in this thesis. The publications discuss in detail the design and optimization of multichannel magnetometers; also, an example is given how the simultaneously measured signals can be utilized to get more reliable results. In the six last papers, the design and fabrication of thin-film SQUID sensors is described. Particular care is exercised to ensure reliable operation and to eliminate excess noise caused by parasitic elements inevitably present in practical devices.

# 1 Basic Concepts and Methods of Neuromagnetism

## 1.1 Cellular Origin of the Electric and Magnetic Fields

The human brain contains on the order of  $10^{11}$  nerve cells or neurons. A typical neuron consists of the soma or the cell body, the axon and the dendrites. Typically, the soma has a diameter ranging from a few micrometers to  $100\text{ }\mu\text{m}$ . The axon, which is a few micrometers in diameter but which may be several millimeters long, is a major fiber emanating from the cell body. The dendrites are smaller and shorter fibers with numerous branches. They can be considered as the incoming fibers of the neuron and the axon as the outgoing fiber. Each axon is usually extensively branched near its ends, and these branches make contacts to the dendrites or to somas of other neurons via special joints, the synapses.

The cell membrane between the extracellular and intracellular fluid of a neuron can selectively pass ions, and it is also capable of actively maintaining concentration differences of various ions. In the resting state, there is a voltage of  $-70\text{ mV}$  between the inside and the outside of the neuron. During an action potential, which propagates along the axon, the transmembrane ionic permeability is suddenly increased, leading to a net inward current and a rapid depolarization, followed by an outward ionic current and restoration of the resting potential. The action potential is an all-or-none event which carries information along the axon, coded in the firing rate of the neuron. When an action potential arrives at the synapse, transmitter molecules are released into the synaptic cleft. After these molecules have been captured by the receptors at the postsynaptic cell membrane, the ionic permeability of the membrane increases. A net current flows through the postsynaptic membrane, and a graded change in the voltage, the so called postsynaptic potential (PSP) results. The PSP may be either excitatory or inhibitory. If the sum of PSPs in the dendrites and in the soma exceeds a certain threshold, an action potential is created, propagating further along the axon to the next synapse. For a detailed description of neural electrical events, see, for example, the book by Kuffler *et al.* [2]. The transmission of information is illustrated in Fig. 1.1.

To a first approximation, the PSP is like a current dipole, oriented along the dendrite, and the action potential may be described by means of a current quadrupole. Magnetic fields detectable outside the head are produced only when a large number of neurons act in concert: typically, the strength of a PSP current dipole is  $10^{-14}\text{ Am}$  [1], whereas on the basis of the measured magnetic fields, it may be estimated that the total current dipole moment is of the order of  $10^{-9}$ – $10^{-8}\text{ Am}$ .

The observed magnetic fields are believed to be largely due to PSPs in the so called pyramidal cells, which are oriented perpendicular to the cerebral cortex, as

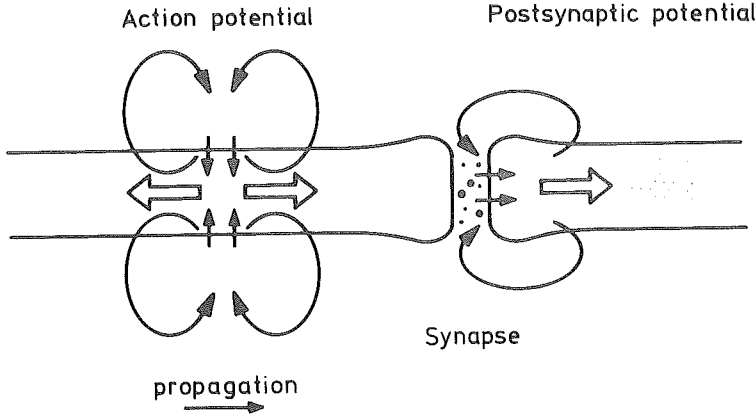


**Figure 1.1.** Schematic illustration of the transmembrane, intracellular, and extracellular currents associated with a propagating action potential in the axon and with an excitatory postsynaptic potential in the dendrite. The postsynaptic potential is triggered by the release of transmitter molecules across the synapse.

illustrated schematically in Fig. 1.2. Fields due to other neurons, being randomly oriented, tend to be averaged out; the field due to an action potential is quadrupolar, and thus it diminishes rather rapidly as a function of distance. In addition, the action potentials last only a few milliseconds whereas the duration of PSPs is an order of magnitude longer.

## 1.2 Modeling

Currents flowing in neural tissue are customarily divided into primary currents  $\vec{J}_p(\vec{r})$ , located at the sites of biological activity, and to volume currents  $\vec{J}_v(\vec{r}) = \sigma(\vec{r})\vec{E}(\vec{r}) = -\sigma(\vec{r})\nabla V(\vec{r})$ , where  $\sigma(\vec{r})$  is the conductivity of the tissue,  $\vec{E}(\vec{r})$  is the electric field, and  $V(\vec{r})$  is the electric potential;  $\sigma(\vec{r})$ ,  $\vec{E}(\vec{r})$  and  $V(\vec{r})$  must be considered on a macroscopic length scale, of the order of 1 mm.

Let us now assume that the volume conductor  $G$ , where the biological sources are located, is bounded and piecewise homogeneous. Let further the subregions of conductivities  $\sigma_i$  be separated by surfaces  $S_j$ . Then, for  $\vec{r}$  not on any surface  $S_j$ , the magnetic field is given by [3]

$$\vec{B}(\vec{r}) = \frac{\mu_0}{4\pi} \left( \int_G \vec{J}_p(\vec{r}') \times \frac{\vec{r} - \vec{r}'}{|\vec{r} - \vec{r}'|^3} dv' - \sum_{j=1}^n (\sigma'_j - \sigma''_j) \int_{S_j} V(\vec{r}') d\vec{S}_j \times \frac{\vec{r} - \vec{r}'}{|\vec{r} - \vec{r}'|^3} \right) \quad (1.1)$$

and the electric potential  $V$  is given by [4]

$$\sigma(\vec{r})V(\vec{r}) = \frac{1}{4\pi} \left( \int_G \vec{J}_p(\vec{r}') \cdot \frac{\vec{r} - \vec{r}'}{|\vec{r} - \vec{r}'|^3} dv' - (\sigma'_j - \sigma''_j) \int_{S_j} V(\vec{r}') d\vec{S}_j \cdot \frac{\vec{r} - \vec{r}'}{|\vec{r} - \vec{r}'|^3} \right) \quad (1.2)$$

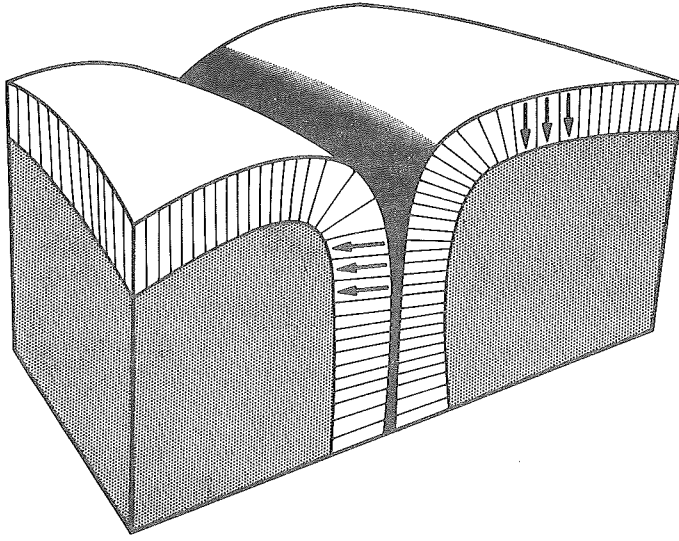


Figure 1.2. Orientation of the source currents due to postsynaptic potentials, with respect to the surface of the cerebral cortex.

for  $\vec{r}$  in  $G$  but not on any surface  $S_j$ . Here,  $\sigma'_j$  and  $\sigma''_j$  denote the conductivities on the inner and outer sides of  $S_j$ , respectively. It may be noted that the first terms in Eqs. (1.1) and (1.2) have the same form as the solution for  $\vec{B}$  and  $V$  due to  $\vec{J}_p(\vec{r})$  in a homogeneous space, whereas the contributions of the inhomogeneities, given by the second terms, may be calculated as if they were due to surface current distributions  $(\sigma'_j - \sigma''_j)V(\vec{r}')\vec{n}(\vec{r}')$ , where  $\vec{r}'$  is on an interface  $S_j$ , and  $\vec{n}(\vec{r}')$  is the outer unit normal vector of  $S_j$  at  $\vec{r}'$ . These hypothetical surface currents are often referred to as secondary currents.

The primary current distribution is usually modeled by one or more current dipoles; the volume conductor is often modeled by a sphere with a conductivity profile  $\sigma(r)$ . This spherically symmetric geometry has several important consequences: 1) radial dipoles, together with their volume currents, do not generate any magnetic field outside the conducting body; 2) the radial component of the magnetic field is produced by the tangential component of the primary current density only, and 3) both radial and tangential magnetic field components are independent of the conductivity profile  $\sigma(r)$ .

For a radial primary current element the resulting current distribution will have cylindrical symmetry around the axis passing through the center of the sphere and parallel to the current. Thus, the magnetic field lines can only be circles around that axis. Since the total current passing through any contour surrounding the whole sphere is zero, it follows from the Ampère law that the field outside the conductor must be zero.

The fact that MEG is insensitive to radial current sources is, however, not a



serious drawback since most of the cortical surface is in the fissures. Because the pyramidal cells are oriented perpendicular to the cortex, the flow of the primary current in the fissures is tangential to the surface of the head.

By taking the dot product of the radial unit vector  $\vec{e}_r$  with Eq. (1.1), it is readily seen that the radial component of the magnetic field in a spherically symmetric volume conductor may be obtained from the primary current density alone. In the second term we get a scalar triple product which vanishes because the unit normals of the interfaces  $S_j$  are parallel to  $\vec{e}_r$ . Consequently, if the primary source is a current dipole  $\vec{Q}\delta(\vec{r}-\vec{r}_0)$  located at  $\vec{r}_0$ , the radial component is given by

$$B_r(\vec{r}) = \frac{\mu_0}{4\pi} \frac{\vec{Q} \times (\vec{r} - \vec{r}_0)}{|\vec{r} - \vec{r}_0|^3} \cdot \vec{e}_r. \quad (1.3)$$

The calculation of all components of the magnetic field outside the conducting body due to a current dipole  $\vec{Q}$  in a spherically symmetric conductor can be accomplished by integrating the scalar potential of the magnetic field along a radius vector and making use of Eq. (1.1) [5]. The result is

$$\vec{B}(\vec{r}) = \frac{\mu_0}{4\pi} \frac{F(\vec{r}, \vec{r}_0) \vec{Q} \times \vec{r}_0 - \vec{Q} \times \vec{r}_0 \cdot \vec{r} \nabla F(\vec{r}, \vec{r}_0)}{F(\vec{r}, \vec{r}_0)^2}, \quad (1.4)$$

where  $F(\vec{r}, \vec{r}_0) = a(ra + r^2 - \vec{r}_0 \cdot \vec{r})$  and  $\nabla F(\vec{r}, \vec{r}_0) = (r^{-1}a^2 + a^{-1}\vec{a} \cdot \vec{r} + 2a + 2r)\vec{r} - (a + 2r + a^{-1}\vec{a} \cdot \vec{r})\vec{r}_0$ , with  $\vec{a} = (\vec{r} - \vec{r}_0)$ ,  $a = |\vec{a}|$ , and  $r = |\vec{r}|$ . From Eq. (1.4) it is clear that the magnetic field does not depend on the conductivity profile  $\sigma(r)$ .

Although the tangential field components do receive non-zero contributions from the volume currents, the effect is such that the tangential field component outside the conductor can be obtained without explicit reference to volume currents, as long as spherical symmetry is maintained. Therefore, the usefulness of tangential components or other than axial derivatives ( $\partial B_r / \partial r$ ) is not reduced [1].

The widely used spherical conductor model is, of course, a crude approximation of the human head. In a series of numerical simulations carried out by Hämäläinen and Sarvas [6], the magnetic fields were compared in three different volume conductor models. They included a realistically head-shaped three-layer model, consisting of the brain tissue, the skull, and the scalp, a homogeneous body having the shape of the inner surface of the skull, and the sphere model. Neglecting the skull and the scalp in the second model seems justifiable, since the conductivity of the skull is almost two orders of magnitude smaller than that of the brain tissue and the scalp. It was found that in regions with no abrupt changes of local curvature, e.g. in the occipital and parietal areas, the sphere model approximates the field values within a few percent, with the radius of curvature fitted to the local curvature. In the frontotemporal area, where deviations from sphericity are large, the spherical model badly fails to reproduce the correct field pattern. However, the homogeneous head model is an excellent approximation even there. Since the potentials need not be found on the skull or on the scalp the homogeneous model requires much less computer time than the full three-layer model.

### 1.3 Data Analysis

In studies of evoked responses, the fields elicited by peripheral stimulation are measured at several locations over the head. The stimulus can be, for example, short tones delivered to the subject's ear; the field is measured from an area of approximately 200 cm<sup>2</sup>, using 30 – 40 points. The maximum amplitudes of these evoked responses are typically 50 – 500 fT; in comparison, the noise levels of most magnetometers are between 5 and 50 fT/ $\sqrt{\text{Hz}}$ . Usually, a measurement bandwidth extending from about 0.1 Hz up to a few hundred Hz is used. It is common to assume that the measured signals consist of the correct value plus Gaussian noise, and the signal-to-noise ratio is usually augmented by averaging many, typically of the order of 100 evoked responses. The MEG data are normally viewed by plotting the isocontour maps of the field distribution as a function of time. A simple field pattern can often be accounted for by a current dipole, the parameters of which are found by least-squares fitting. Thus, one may trace the equivalent source location with a millisecond time resolution.

In the mathematical analysis the estimates of the equivalent dipole parameters (location, orientation, and magnitude), obtained from the least-squares fit, are random variables with the mean coinciding with the true dipole. By evaluating the confidence intervals for the parameters, one may obtain a quantitative measure of the reliability of the estimates. The confidence region in the parameter space may be defined as being the smallest set of parameter values making up the given total probability of the *a posteriori* distribution, i.e. the probability distribution of the dipole parameters yielding a certain measurement result [7].

Assume that the measured field values are  $\mathbf{b} = (b_1 \dots b_n)^T$ , where  $T$  denotes the transpose. The unknown current distribution is assumed to be characterized by a parameter vector  $\mathbf{x} = (x_1 \dots x_m)^T$ . For example,  $\mathbf{x}$  may comprise the components and position coordinates of a current dipole in a sphere. Before and after the measurement, the knowledge of  $\mathbf{x}$  is described by the *a priori* and *a posteriori* distributions  $f_{\text{pr}}(\mathbf{x})$  and  $f_{\text{post}}(\mathbf{x})$ , respectively. If no detailed information about the distribution of  $\mathbf{x}$  exists,  $f_{\text{pr}}(\mathbf{x})$  can be chosen as a uniform distribution in a set containing all the possible values of  $\mathbf{x}$ . Let us further assume that  $\mathbf{b} = \mathbf{g}(\mathbf{x}) + \epsilon$ , where  $\mathbf{g}(\mathbf{x})$  is the generally nonlinear function giving the magnetic field for the chosen set of model parameters and  $\epsilon$  is a Gaussian noise vector which is independent of  $\mathbf{x}$ , and has a covariance matrix  $\Sigma = E(\epsilon\epsilon^T)$  and a mean  $E(\epsilon) = 0$ . Here,  $E$  denotes the expectation value. Then, the *a posteriori* distribution for a measurement  $\mathbf{b}_0$  can be written [8]

$$f_{\text{post}}(\mathbf{x}) = C_0 f_{\text{pr}}(\mathbf{x}) \exp \left( -\frac{1}{2} [\mathbf{b}_0 - \mathbf{g}(\mathbf{x})]^T \Sigma^{-1} [\mathbf{b}_0 - \mathbf{g}(\mathbf{x})] \right), \quad (1.5)$$

where  $C_0$  is a normalization constant. For a uniform *a priori* density, the maximum likelihood estimate is thus obtained by minimizing the argument of the exponential, i.e., by the least-squares search.

Since  $\mathbf{g}(\mathbf{x})$  is nonlinear for the current dipole, the confidence set of  $\mathbf{x}$  in the parameter space is tedious to compute [7]. However, using linearization in the vicinity of the maximum likelihood estimate of the parameters, i.e. the least squares solution, the confidence region can be conveniently calculated. The function  $\mathbf{g}(\mathbf{x})$

is approximated by  $\mathbf{g}(\mathbf{x}_0) + \mathbf{J}(\mathbf{x} - \mathbf{x}_0)$ , where  $\mathbf{J}$  is the Jacobian matrix of  $\mathbf{g}(\mathbf{x})$  at  $\mathbf{x}_0$ . By making the spectral decomposition  $\mathbf{J}^T \Sigma^{-1} \mathbf{J} = \mathbf{V}^T \Lambda^{-2} \mathbf{V}$ , where  $\mathbf{V}$  is an orthogonal matrix and  $\Lambda$  is diagonal, it can be shown that the  $p$ -percentage confidence region is given by the  $m$ -dimensional hyperellipsoid [5]

$$(\mathbf{x} - \mathbf{x}_0)^T \mathbf{V}^T \Lambda^{-2} \mathbf{V} (\mathbf{x} - \mathbf{x}_0) < r^2. \quad (1.6)$$

Here,  $r^2$  is the  $p$ -percent point of the  $\chi_m^2$  distribution. The ellipsoid is centered at  $\mathbf{x}_0$ , and its half-axes are given by  $r\lambda_i \mathbf{v}_i$ , where  $\lambda_i$  and  $\mathbf{v}_i$  are the eigenvalues and eigenvectors of  $\mathbf{J}^T \Sigma^{-1} \mathbf{J}$ . The confidence intervals for the parameters  $x_i$  are then given by the edges of a rectangular box containing the confidence ellipsoid and having its faces parallel to the coordinate planes.

A single tangential current dipole in a spherical conductor has five parameters, three position coordinates and two strength components in the tangential plane. The confidence limits are generally largest in the radial direction, i.e., the depth, and the smallest in the direction perpendicular to the dipole in the tangential plane, as shown by simulations [9,10] and by calculations from measured data [11,12]. The values of the confidence limits are, of course, affected by the noise level, but they also depend on the depth of the dipole and on the measurement grid.

## 1.4 Spatial Resolution of MEG

As discussed above, confidence limit calculations provide a quantitative measure of the reliability for the estimates. In addition, they may also be utilized to give an estimate of the spatial locating accuracy of MEG, which can, for example, be used as a figure-of-merit in comparing various magnetometer arrays designed to be used in neuromagnetism, as in Publications 3 and 4.

The spatial resolution of MEG may also be considered from a slightly different point of view by evaluating the minimum resolvable separation between two dipoles, based on a statistical test whether two measured field distributions differ significantly. For example, for a spatial resolution of 3 mm of a typical 10 nA cortical source, a signal-to-noise ratio of about 10 is needed [9].

The spatial resolution of MEG in locating superficial dipole sources is thus of the order of a few millimeters. For deeper sources located, for example, 40 – 50 mm below the scalp, the resolution is substantially worse. This is largely due to the fact that, for example, the signals from thalamic sources or from the brainstem are very weak. Thus, MEG is best suited for studies of cortical sources; however, in certain cases, as in epilepsy, deep sources may be very strong, and then the magnetoencephalographic method offers a considerable locating accuracy.

The potential distribution over the head caused by the brain activity, the EEG, has been studied for over 100 years. EEG has provided a valuable clinical diagnostic tool; however, the actual locating of sources on the basis of the potential distribution on the scalp is difficult. The relation of MEG and EEG in their ability to locate current sources is best illustrated by the volume conductor model calculations [6] referred to earlier. The measured magnetic field is caused by currents that flow along approximately undistorted paths in the brain tissue where

the current dipole is located, while the scalp potentials measured in EEG suffer from distortion caused by local irregularities of the extracerebral conductivities. This fact largely explains the better spatial accuracy of magnetic measurements. In addition, the EEG receives contribution from radial sources. An example of how the magnetic field patterns due to three simultaneously active dipoles are clearly distinct whereas the electric potentials are smeared out, making it difficult to locate their sources, is given by Kaukoranta *et al.* [13].

## 2 Josephson Junctions

### 2.1 Phase Coherence

Quantum-mechanical phase coherence in superconductors forms the basis of operation of SQUIDS. The superconducting state can be characterized by an order parameter  $\Psi(\vec{r}) = |\Psi(\vec{r})|e^{i\varphi(\vec{r})}$  which shows phase coherence over macroscopic distances. For example, by calculating the phase difference  $\Delta\varphi$  around a loop of a superconductor in a magnetic field  $\vec{B} = \nabla \times \vec{A}$ , one obtains the well-known condition [14]

$$\frac{\Delta\varphi}{2\pi} = \frac{2e}{h} \Phi, \quad (2.1)$$

where  $\Phi = \oint \vec{A} \cdot d\vec{l} = \int \vec{B} \cdot d\vec{S}$  is the flux threading the loop. Since the phase difference must be an integer multiple of  $2\pi$ , the flux through the ring is quantized in units of  $\Phi_0 = h/2e = 2.07 \times 10^{-15}$  Wb, the flux quantum.

The Josephson effect is another manifestation of quantum phenomena in superconductors. In 1962, Josephson predicted [15] the existence of phase coherence between two superconductors if they are coupled through a weak tunnel barrier contact. In particular, there can be a tunneling supercurrent. The Josephson effect may be described by

$$I = I_0 \sin \theta \quad (2.2)$$

and

$$\frac{d\theta}{dt} = \frac{2e}{h} V = \frac{2\pi}{\Phi_0} V, \quad (2.3)$$

where  $I$  is the tunneling supercurrent,  $I_0$  the critical current,  $\theta$  the phase difference, and  $V$  the voltage across the Josephson junction. Eq. (2.3) implies that in the presence of a voltage, the current across the junction oscillates with the frequency  $V/\Phi_0$  where  $1/\Phi_0 = 483.6$  MHz/ $\mu$ V. Eq (2.2) is actually only approximate; deviations from this relation are observed.

In addition to superconductor-insulator-superconductor (SIS) tunnel junctions, the Josephson effect is also observed in various other weak contacts, such as the superconductor-normal-superconductor (SNS) or superconductor-semiconductor-superconductor interface, the proximity effect bridge, in the Dayem bridge, and in the point contact. Many theoretical and experimental aspects of the various types of weak links are discussed extensively in the review by Likharev [16]; for another survey of the Josephson effect, see also the book by Barone and Paterno [17]. In this thesis, only SIS tunnel junctions are considered.

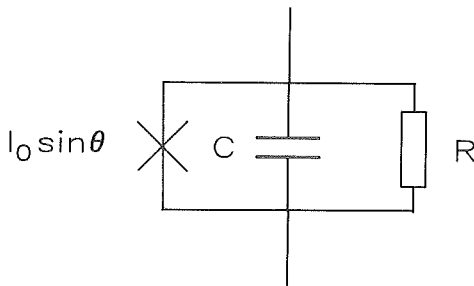


Figure 2.1. The resistively shunted junction (RSJ) model of a Josephson junction.

## 2.2 Electrical Characteristics of Josephson Junctions

A real Josephson junction may be characterized by the resistively shunted junction (RSJ) model shown in Fig. 2.1, which consists of a shunt resistance  $R$  and a junction capacitance  $C$  in parallel with an ideal junction [18,19]. The differential equation for the current  $I$  through this junction can be written as

$$I = \frac{C\Phi_0}{2\pi} \frac{d^2\theta}{dt^2} + \frac{\Phi_0}{2\pi R} \frac{d\theta}{dt} + I_0 \sin \theta \quad (2.4)$$

or, in dimensionless form, where voltage  $v$  is measured in units of  $I_0 R$ , current  $i$  in  $I_0$ , flux  $\phi$  in  $\Phi_0$ , and time  $\tau$  in units of  $\Phi_0/2\pi I_0 R$ :

$$\beta_c \frac{d^2\theta}{d\tau^2} + \frac{d\theta}{d\tau} = -\frac{d}{d\theta}(-i\theta - \cos \theta), \quad (2.5)$$

where  $\beta_c = 2\pi I_0 R^2 C / \Phi_0$  is called the Stewart-McCumber parameter. This differential equation is analogous to the equation of motion of a particle of mass  $\beta_c$ , moving in a viscous medium under the influence of gravity down a tilted washboard shaped surface, the voltage corresponding to the velocity of the particle.

Depending on the value of  $\beta_c$ , the Josephson junction exhibits two different types of behavior. At small  $\beta_c$ , i.e., when the junction is well damped, the current-voltage characteristics is nonhysteretic, whereas at parameter values  $\beta_c > 1$  the inertia of the system causes hysteresis [18,19]. When  $I < I_0$ , the system has two solutions, the zero-voltage state and the quasiparticle tunneling state [20]. To describe the junction properly, the constant conductance  $1/R$  in the RSJ model should be replaced by a voltage-dependent quasiparticle conductance. Examples of current-voltage characteristics of tunnel junctions are shown in Fig. 2.2.

In a tunnel junction at bias currents well above  $I_0$ , the critical current  $I_0$  and the tunneling resistance  $R$  are related by the Ambegaokar-Baratoff formula [21]

$$I_0 R = \frac{\pi k_B T}{e} \Delta_1(T) \Delta_2(T) \sum_{l=0, \pm 1, \dots} \{[\omega_l^2 + \Delta_1^2(T)][\omega_l^2 + \Delta_2^2(T)]\}^{-\frac{1}{2}}, \quad (2.6)$$

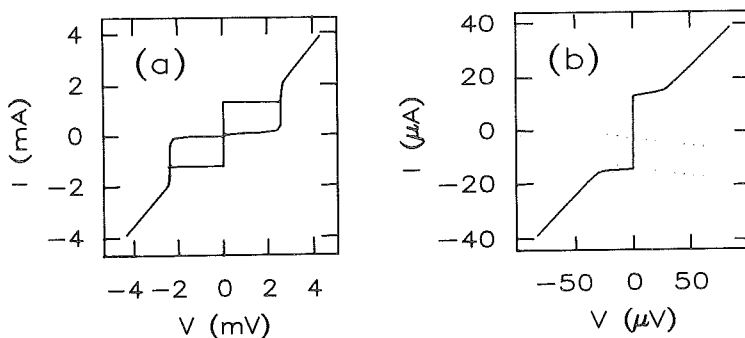


**Figure 2.2.** Current-voltage characteristics of Josephson junctions, measured from  $10 \times 10 \mu\text{m}^2$  Nb-Nb oxide-PbInAu tunnel junctions. (a) Hysteretic junction. (b) Nonhysteretic junction, shunted by an external resistor  $R$ .

where  $\Delta_1(T)$  and  $\Delta_2(T)$  are the superconductor energy gaps,  $\omega_l = \pi k_B T(2l + 1)$ , and  $T$  is the temperature. For a symmetrical junction with  $\Delta_1(T) = \Delta_2(T) = \Delta(T)$ , the sum can be calculated analytically, and Eq. (2.6) reduces to

$$I_0 R = \frac{\pi \Delta(T)}{2e} \tanh\left(\frac{\Delta(T)}{2k_B T}\right). \quad (2.7)$$

For a Nb-Nb oxide-Pb junction at 4.2 K, the value of  $I_0 R$  is approximately 1.6 mV [22,23]. This experimentally determined value is 0.7 times that predicted from the Ambegaokar-Baratoff formula. The difference is due to strong-coupling and proximity effects, not taken into account in the original theory.

In thin-film tunnel junctions the capacitance of the structure is considerable. For example, in Nb-Nb oxide-Pb rectangular tunnel junctions an experimentally determined relation is [24]

$$1/C_s = (0.105 \pm 0.010) - (0.0045 \pm 0.0015) \ln j_c, \quad (2.8)$$

where  $C_s$  is the specific capacitance in  $\mu\text{F}/\text{cm}^2$  and  $j_c$  the critical current density in  $\text{A}/\text{cm}^2$ . Thus, for  $j_c = 1000 \text{ A}/\text{cm}^2$ ,  $C_s = 13 \mu\text{F}/\text{cm}^2$ . This is due to the high dielectric constant of  $\text{Nb}_2\text{O}_5$  ( $\epsilon = 30 - 100$  [25]) and the thinness of the barrier. Accordingly, practically all tunnel junctions, except possibly some very-small-area junctions approaching point-contact type, are inherently hysteretic. Therefore, an external shunt resistor must usually be connected in parallel with the junction.

The critical current in tunnel junctions depends exponentially on the barrier thickness  $d$ . For Nb-Nb oxide-Pb junctions, experimental dependencies  $e^{-0.31d}$  for thermally grown oxide barriers [26] and  $e^{-0.78d}$  for rf-plasma-oxidized barriers [22] have been reported. In the latter case, a junction with a critical current density of  $1000 \text{ A}/\text{cm}^2$  implies an oxide barrier thickness of 13 nm, for example. Thus the fabrication of the barrier is very critical; small parameter variations may cause large deviations in junction characteristics.

The observed critical currents of Josephson junctions can be substantially lower than predicted by Eq. (2.6). For example, a magnetic field parallel to the plane of the junction modulates the critical current in a manner resembling Fraunhofer diffraction [27]

$$I_{\max} = I_0 \left| \frac{\sin(\pi\Phi/\Phi_0)}{\pi\Phi/\Phi_0} \right|, \quad (2.9)$$

where  $\Phi$  is the magnetic flux through the area limited by the London penetration lengths of the superconducting electrodes and the junction width. A field perpendicular to a thin film junction may also reduce the observed critical current: a trapped flux quantum suppresses the critical current of the junction by the fraction  $\pi(6\lambda_L)^2/A$ , where  $\lambda_L$  is the London penetration depth and  $A$  the junction area [28].

A further aspect causing reduction in the observed critical current, especially at low current densities, is the finite lifetime of the zero-voltage state. As mentioned earlier, the junction is analogous to a particle in a metastable potential well, from which it can escape via thermal activation or via quantum tunneling. Thermal activation, which is the dominant mechanism except at very low temperatures, has been studied theoretically [29,30] as a function of the critical current, the bias current, the junction capacitance, and the temperature. According to the thermal activation model [29] the lifetime of the metastable state is

$$\tau = \frac{2\pi\Phi_0 C}{I_0} \frac{1}{(1-x^2)^{\frac{1}{4}}} e^{E/k_B T}. \quad (2.10)$$

Here,  $E = I_0\Phi_0[x(2\arcsin x - \pi) + 2\cos(\arcsin x)]$  is the height of the potential barrier and  $x = I/I_0$ , where  $I$  is the bias current. Because of this exponential dependence, only a small fraction of the current may actually be observed in a practical measurement setup at low critical currents, below 10  $\mu\text{A}$ , for example. This dependence was observed experimentally for our junctions fabricated with three different oxidation methods in Publication 7. The fact has practical implications in the design of Josephson devices; it must be taken into account as a boundary condition limiting the applicable range of parameter values.

In addition to the critical current and the normal-state tunneling resistance, the properties and the quality of tunnel junctions are characterized by the subgap leakage current. A simple but useful measure of this current is provided by the parameter  $V_m$ , defined as the product of the critical current and the linear tunnel resistance at 2 mV [22]. This method is especially useful in comparing the effects of various process conditions; when  $V_m \geq 25$  mV the junction is of high quality [31].

## 2.3 Fabrication of Thin-Film Tunnel Junctions

In this section, the fabrication of thin-film SIS tunnel junctions is described briefly, limiting the discussion to conventional superconducting electrode materials, Nb, Pb, and compounds containing these metals.

Traditionally, the superconducting structures of SQUIDs have been fabricated from pure Nb and Pb alloys that contain about 10 % of Au, In or both. Pure



lead is not used because it is easily corroded. In a conventional structure, the base electrode of the junction is fabricated of Nb, the top electrode of Pb alloy, and the tunnel barrier is formed by oxidizing the Nb surface. The area of the junction is defined by an opening in the insulation layer between the electrodes. The fabrication and properties of these structures have been discussed in detail, for example, in the review by Broom *et al.* [22]. During the last few years, new all-refractory-material junctions have been introduced, utilizing all-Nb, NbN, and NbGe electrodes. Together with the use of "artificial" tunnel barriers like  $\text{Al}_2\text{O}_3$  and  $\text{MgO}$ , they have provided superior properties, such as better stability, wider operating temperature range, good critical current uniformity and reproducibility, and high values of the parameter  $V_m$ . For recent reviews, see, for example Refs. [31] and [32].

Electron-gun evaporation and sputtering are the main methods in depositing thin films. Especially sputtering has become popular. For example, in depositing Nb films, the high melting temperature of Nb, the requirement of heating the substrate to avoid strains in the films, and the easy gettering of impurities make evaporation difficult; in addition, control of film thickness and deposition rate is easier in sputtering.

The films are patterned using etching through photolithographically defined resist masks. Chemical wet etching is seldom employed today; instead, reactive ion [33] and ion beam etching are used [34]. Another possibility is to apply lift-off techniques. In this method, a photoresist layer is first coated over the substrate and patterned. Following film deposition the resist is removed, thereby lifting off those parts of the film which were on the resist. The minimum linewidths in both methods, using optical photolithography, are typically a few micrometers. For finer details, electron-beam lithography must be used; with it submicron structures are possible.

The use of several photolithographic mask layers with fine details requires accurate alignment. Because of the overhead in the dimensions, necessary for alignment, very small junctions are difficult to fabricate in a well-controlled manner. In order to avoid problems, self-alignment techniques for junction formation have been developed [35]–[39]. In these methods, the junction is formed on the whole wafer and patterning is carried out afterwards; using this technique it is also possible to reduce the number of masks required.

In window-type junctions capacitances are relatively large. To reduce the junction area, edge junctions have been introduced [40,41]. In this structure, the edge of the film is etched to be oblique, the top of the film is insulated, and the actual junction is formed by oxidizing the edge. By this method, junctions whose other dimension is of the order of the film thickness can be obtained. Another method is to form the junction between two vertical side-by-side edges of the film [42]. The characteristics of junctions formed by the latter method resemble those of point-contact junctions; no external shunting is necessary.

The tunnel barriers fabricated and studied in this thesis (Publications 6, 7, 8, and 10) are formed by oxidizing the niobium base electrode. The most widely used method is plasma oxidation, either using rf [43] or dc plasma [44,45]. For better process control, normally a mixture of Ar and  $\text{O}_2$ , typically containing 95% of Ar, is used as the working gas. In our SQUIDS, dc plasma oxidation is used;

the fabrication is described in detail in Papers 6 and 10.

The entire fabrication process is quite complex. A SQUID has typically ten different mask layers, hence ten vacuum depositions with lithographic patterning are required. Consequently, the yield of devices having the desired characteristics can be very low. Formation of the tunnel barrier is the most critical phase; furthermore, reliable fabrication of small structures resulting from the optimization of SQUIDs requires highest quality lithography.

The exponential dependence of the critical current on the oxide barrier thickness requires very accurate control of the oxidation. Inhomogeneities in the plasma lead to a large spread of the critical current, and the run-to-run variability can in the worst case be over an order of magnitude. Microshorts can also easily form in the thin tunnel barrier.

The oxide layer forming on top of the niobium has a complex structure. Between the Nb surface and the bulk  $\text{Nb}_2\text{O}_5$ , suboxides  $\text{NbO}_x$  are formed, which can increase the leakage current and reduce the observed critical current. Also, oxygen dissolved in the Nb electrode from the oxide layer lowers the critical temperature.

To remove uncontrolled thermally grown native oxides, the Nb surface is cleaned before oxidation with Ar using rf plasma discharge or an ion beam. For the quality of the junctions, especially for obtaining a large value of  $V_m$ , the precleaning step is very important. It has been shown that during this process a niobium oxycarbide transition layer  $\text{NbO}_x\text{C}_y$  forms on top of the Nb from the remanent gases in the vacuum system and from the photoresist. Because of this transition layer below the actual  $\text{Nb}_2\text{O}_5$  oxide, the tunnel barrier is better defined and the formation of oxides other than  $\text{Nb}_2\text{O}_5$  is reduced; in addition, the diffusion of oxygen into the Nb is decreased [23],[46]–[48]. A small amount of carbon in the residual gases is therefore essential for the formation of high-quality junctions. On the other hand, large concentrations of impurities have catastrophic consequences on the junction quality. In ultra-high-vacuum systems, the formation of the oxycarbide transition layer has been helped by deliberately letting in methane.

The ion beam preclean has also disadvantages. The use of high ion beam energies, necessary for better cleaning, damages the Nb surface, leading to a faster and not well controlled oxidation rate. Because of ion bombardment during the preclean, the photoresist used in the lift-off process can also be damaged; as a result it may not lift off properly. In addition, during the preclean the substrate heats; during initial stages of the plasma discharge preparation the substrate will oxidize spontaneously. In the fabrication procedure used for our SQUIDs this uncontrolled oxide was a severe problem; to avoid it, the substrates are allowed to cool down to ambient temperature in high vacuum before the oxidation.

Ion beam oxidation offers an interesting alternative for forming the oxide tunnel barrier [41,49,50]. In this technique, an argon-oxygen ion beam is directed to the Nb surface. The advantage is that the energy of the ions and the ion flux and thus the resulting oxide thickness can be well controlled. As in the rf plasma process, a steady state between the oxidation and the sputtering by argon can be achieved, as demonstrated in Publication 8.

In addition to the junction formation, the lithographic processes of the films require utmost care. For example, pinhole defects in the insulator films cause short circuits. They can be avoided using double-layers with different masks, but with

the cost of an extra fabrication step with vacuum deposition and lithography. Long and very narrow conductors, which are necessary in signal coupling coils of well optimized SQUIDS, are difficult to fabricate; small dust particles can easily cause discontinuities in the films. In multilayer structures, conductors must cross over films, and to ensure proper step coverage each successively deposited layer must be thicker than the ones below. Furthermore, possible left-overs from patterning of previous films may also cause discontinuities. For example, during film deposition material is backscattered on the edges of the photoresist stencils used in lift-off; the resulting thin sheet on the edge is partly attached to the substrate and thus it may not be completely removed with the resist. The material on the edges must be etched away before lift-off; however, at the same time the step coverage of cross-overs is weakened.

## 3 SQUID Magnetometers

### 3.1 The rf SQUID

The rf SQUID, which consists of a superconducting ring containing one Josephson junction, was introduced by Silver and Zimmerman in 1967 [51]. During the subsequent years, it gradually became a popular many-purpose high-sensitivity magnetic field sensor. The original point-contact structures have been replaced by thin films, and commercial rf SQUID sensors have been available for a long time from several manufacturers. Typically, the equivalent flux noise of an rf SQUID is  $10^{-4} \Phi_0/\sqrt{\text{Hz}}$ . Careful optimization and the use of higher operating frequencies than the standard 10 – 20 MHz have improved noise levels by an order of magnitude [52]. In this section, the rf SQUID will be briefly discussed; later, the discussion is concentrated on the dc SQUID only, since most of the development work described in this thesis is devoted to the dc SQUID.

For a superconducting ring containing one Josephson junction, the flux quantization condition, Eq. (2.1), is modified to  $\Delta\varphi = \theta - 2\pi\Phi/\Phi_0 = 2\pi n$ , where  $\theta$  is the phase difference across the Josephson junction,  $n$  is an integer, and  $\Phi$  the flux threading the ring. Consequently, the external applied flux  $\Phi_{\text{ext}}$  and the net flux  $\Phi$  through the ring are linked via the relation

$$\Phi = \Phi_{\text{ext}} - LI_0 \sin \frac{2\pi\Phi}{\Phi_0}, \quad (3.1)$$

where  $L$  is the inductance of the ring. If  $2\pi LI_0 < \Phi_0$ , Eq. (3.1) is single-valued whereas for  $2\pi LI_0 > \Phi_0$  it is multivalued, showing hysteresis when the applied external flux is swept back and forth. Practical rf SQUIDs are normally operated in this hysteretic mode; an rf flux with a frequency  $f_{\text{rf}}$ , superimposed on the signal flux to be measured, is applied to the SQUID ring via an inductively coupled resonant tank circuit. The energy loss due to hysteresis loops traversed is then sensed in the voltage of the resonant circuit; the effective  $Q$  value of the tank circuit now depends on the rf bias level and on the external flux applied to the SQUID. As a result, with a suitably chosen fixed rf bias, the tank circuit rf voltage varies triangularly as a function of the signal flux, the period being one  $\Phi_0$ . For a detailed explanation on the operation of the rf SQUID, see, for example, Refs. [17] and [53].

When the Josephson junction is modeled with an RSJ equivalent circuit, relation (3.1) is modified to describe the equation of motion for  $\Phi$  in a potential [54]

$$U(\Phi) = \frac{(\Phi - \Phi_{\text{ext}})^2}{2L} - \frac{\Phi_0 I_0}{2\pi} \cos \frac{2\pi\Phi}{\Phi_0}, \quad (3.2)$$

assuming a constant external flux  $\Phi_{\text{ext}}$ . In the hysteretic case, the potential has metastable valleys separated by barriers having their maxima at the points where

$d\Phi/d\Phi_{\text{ext}}$ , calculated from Eq. (3.1), is infinite. Thermal activation and quantum tunneling now cause transitions offset from these critical points; these transitions are seen as random fluctuations in the tank circuit voltage. The noise in rf SQUID has been studied extensively in the literature [54]–[58]; for the intrinsic noise of the SQUID, not taking into account possible contributions of tank circuit losses and of the preamplifier, nor the effects of the non-sinusoidal current-phase relationship of the junction, theory predicts

$$\Phi_n \simeq 0.5 \left( \frac{1}{f_H} \right)^{\frac{1}{2}} \left( \frac{2\pi k_B T}{\Phi_0} \right)^{\frac{2}{3}} L I_0^{\frac{1}{3}} \left( 1 - \left( \frac{\Phi_0}{2\pi L I_0} \right)^2 \right)^{\frac{1}{6}}. \quad (3.3)$$

The flux sensitivity depends inversely on the square root of  $f_H$ . For the rf SQUID, a complete linear equivalent circuit has been developed, from which input and output impedances, the gain of the SQUID, and noise properties as a function of source impedance have been calculated [59].

## 3.2 The Autonomous dc SQUID

### 3.2.1 Operation and Basic Characteristics

The dc SQUID, which is a superconducting ring with two Josephson junctions, was introduced before the rf SQUID [60,61]. The interference effect observed, resembling that of an optical Young's two slit experiment, later led to the use of the acronym SQUID. After the first experiments, the dc SQUID stayed in the background because of the rapid development of the rf SQUID. After the mid 1970's, however, it gradually became clear that the dc SQUID is potentially more sensitive than the rf SQUID [62], and applied work and basic research both shifted toward it. This development was connected with advances in thin-film technology, which allowed reliable fabrication of two tunnel junctions in one device. Since then, very-low-noise dc SQUIDS, with a minimum energy sensitivity below one Planck's constant, have been reported [63]–[65]. The development of dc SQUIDS is reviewed, for example, in Refs. [66] and [67].

The dc SQUID is biased with a current  $I$ , and the voltage  $V$  over the SQUID is measured. An external magnetic flux applied to the SQUID ring couples to the phase differences across the junctions, and a circular current flows in the ring, partially screening the applied flux. Because of this interaction with the external field, the critical current  $I_C$  through the SQUID is modulated; by setting the bias current slightly above the critical current, the voltage  $V$  over the SQUID is modulated with a period of  $\Phi_0$ .

In the following discussion the absence of noise will be assumed; the effects of noise will be considered in the next section.

The basic equivalent circuit for the dc SQUID with the RSJ model for the Josephson junctions is shown in Fig. 3.1. Using dimensionless variables, defined in section 2.2, the differential equations for the dc SQUID may be written [68,69]

$$v = \frac{1}{2} \left( \frac{d\theta_1}{d\tau} + \frac{d\theta_2}{d\tau} \right), \quad (3.4)$$

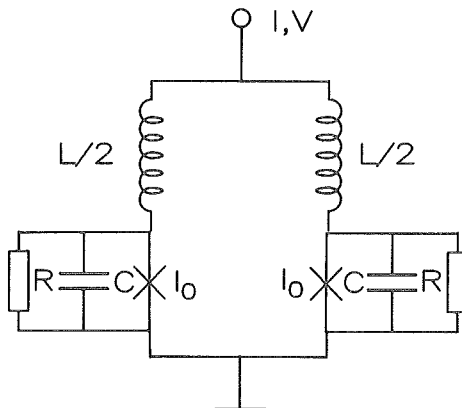


Figure 3.1. The RSJ equivalent circuit of the dc SQUID.

$$j = \frac{\theta_1 - \theta_2 - 2\pi\phi_{\text{ext}}}{\pi\beta}, \quad (3.5)$$

$$\beta_c \frac{d^2\theta_1}{d\tau^2} + \frac{d\theta_1}{d\tau} = \frac{i}{2} - j - \sin\theta_1, \quad (3.6)$$

$$\beta_c \frac{d^2\theta_2}{d\tau^2} + \frac{d\theta_2}{d\tau} = \frac{i}{2} + j - \sin\theta_2. \quad (3.7)$$

Here,  $v$  is the voltage across the SQUID,  $i = i_1 + i_2$  is the bias current,  $j = (i_2 - i_1)/2$  is the current circulating in the loop,  $\theta_1$  and  $\theta_2$  are the phase differences across the junctions,  $\beta = 2LI_0/\Phi_0$  where  $L$  is the total inductance of the loop,  $I_0$  is the critical current of one junction, and  $\beta_c = 2\pi I_0 R^2 C / \Phi_0$ .

These equations cannot, in general, be solved analytically. They were first integrated numerically by Tesche and Clarke [68] and with an analog hybrid computer by Bruines *et al.* [70], neglecting, however, the junction capacitance  $C$ . Later, simulations of the dc SQUID including the junction capacitance have been carried out by several authors, both numerically [71]–[74], and using an analog simulator [69,75]. An example of the current-voltage and flux-voltage characteristics of a real device is shown in Fig. 3.2. The deepest modulation of the critical current is achieved slightly above  $2I_0$ .

A mechanical analog may be applied here again as shown, for example, in Refs. [72] and [76]. We may consider the system as a particle moving under the influence of gravity in a viscous medium on a tilted surface, the form of which is parabolic, having sinusoidal valleys and hills. In contrast to the single junction or the rf SQUID, which were one-dimensional cases, the particle now has two positional degrees of freedom. The parameter  $\beta$  and the external flux determine the shape of the potential, and the parameter  $\beta_c$  again corresponds to the mass of the particle. Customarily, the individual phase variables are replaced by the sum and the difference. The sum phase corresponds to the straight motion of the particle down the potential, its velocity being the voltage over the SQUID,

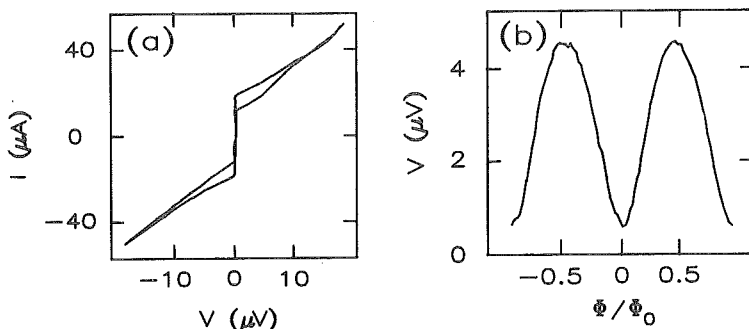


**Figure 3.2.** (a) The current-voltage characteristics measured from a dc SQUID with  $I_0 = 18 \mu\text{A}$  and  $R = 0.5 \Omega$ , corresponding to  $\beta = 1.6$  and  $\beta_c = 0.1$ . The curve is shown for two flux values, having an integer or a half-integer multiple of flux quanta. (b) The corresponding flux-to-voltage characteristics at the bias current  $20 \mu\text{A}$ .

whereas the difference phase corresponds to the sidewise movements of the particle. According to this analog the solutions of the system equations may be divided into three categories: 1) the zero-voltage state where the particle stays in a local minimum, 2) the “running” or single-junction state where it moves down without side movements, and 3) the “beating” state, where the particle has both types of motion. In the normal operation of the SQUID, the running solution is usually assumed, and the beating solution appears as an instability to the single-junction state; both solutions can also co-exist. A numerically determined phase space for the dc SQUID as a function of  $\beta$  and  $\beta_c$  is given in Ref. [73].

The behavior of the critical current modulation, the average circulating current, the average current-voltage characteristics, and the transfer function have been studied extensively as functions of the SQUID parameters by Tesche and Clarke [68], assuming, however, zero junction capacitance. They also included asymmetry of the SQUID in their analysis. The behavior of the dc SQUID was found to be relatively insensitive to quite large asymmetries in the inductances of the two arms, or in the critical currents and shunt resistances of the two junctions.

For calculations, it is often useful to have approximate analytical formulae, which are simple fits to the simulated results [68,74,77], for the key characteristics of the SQUID. The modulation of the critical current, with the junction capacitance neglected, is given by

$$\frac{\Delta I_C}{2I_0} \simeq \frac{1}{1 + \beta}, \quad (3.8)$$

and the average circulating current is

$$J \simeq - \left( \frac{1}{(3 + \beta)} \frac{\Phi_{\text{ext}}}{\Phi_0} - \frac{1}{2} \right) I_0. \quad (3.9)$$

Here,  $\Phi_{\text{ext}}$  is the flux applied to the ring. It must be emphasized that this relation is linearized and accurate only around  $\Phi_{\text{ext}} = \Phi_0/2$ . This approximation, however,

holds still reasonably well at applied fluxes of  $\Phi_0/4$  or  $3\Phi_0/4$ , where the flux-to-voltage transfer function has its maximum and is approximated by

$$G = \frac{\partial V}{\partial \Phi_{\text{ext}}} \simeq \frac{g}{(1 + \beta)} \frac{I_0 R}{\Phi_0}, \quad (3.10)$$

where  $g$  is a constant between 1 and 2; for small capacitances  $g \simeq 2$ .

### 3.2.2 White Noise and Energy Sensitivity

Thermal noise in the shunt resistors  $R$  can be taken into account by adding a noise source term in the Eqs. (3.6) and (3.7). The spectral density of this noise is given in dimensionless units as  $S_R^N = 4\Gamma$ , where  $\Gamma = 2\pi k_B T / I_0 \Phi_0$ . The effect of noise on the SQUID characteristics has been studied extensively in papers cited in the previous section; the current-voltage and flux-to-voltage characteristics become rounded, smearing off sharp edges and transitions between different solutions caused by the large values of  $\beta_c$  and  $\beta$ .

The voltage noise in the SQUID output is usually converted into an equivalent flux noise  $\Phi_n$  by dividing it by the flux-to-voltage transfer function  $G$ . The flux noise has a minimum when the applied flux is  $\Phi_0/4$  or  $3\Phi_0/4$ , where  $G$  is at maximum. At frequencies much less than the Josephson oscillations, the spectral density of the equivalent flux noise is white. Often, the figure-of-merit describing the noise performance of a SQUID is the energy sensitivity

$$\varepsilon_s = \frac{\Phi_n^2}{2L}, \quad (3.11)$$

which has been studied in simulations as a function of  $\beta$  and  $\beta_c$ ;  $\varepsilon_s$  has a minimum when  $\beta \simeq 1$  and  $\beta_c \simeq 1$ . This optimum energy sensitivity is given by

$$\varepsilon_s = 8\gamma k_B T \sqrt{LC}, \quad (3.12)$$

where the factor  $\gamma$  is reported to be 1.5 [69] or 2 [68]. In the former case, the junction capacitance was taken into account in the simulations whereas in the latter case it was not. A plausible explanation for this difference could be the different mixing-down contributions: the capacitance limits the bandwidth of the system and thus reduces the amount of high-frequency noise, mixed down to low frequencies via the nonlinearities of the SQUID.

In addition to mixed-down noise, transitions between multiple modes of the SQUID dynamics, caused by the large values of  $\beta$  and  $\beta_c$ , introduce excess noise. Although the increasing  $\beta_c$  reduces the contribution from the mixed-down noise,  $\beta_c$  should not be allowed to be larger than 1; otherwise, excess noise processes enter via multiple modes.

It is instructive to derive a simple approximate analytical model for the energy sensitivity. Taking into account the voltage noise of the SQUID and the circulating current noise, we get for the equivalent flux noise

$$\Phi_n^2 = 2k_B T \left( \frac{L^2}{R} + \frac{R}{G^2} \right) = \frac{2k_B T}{R} L^2 \left[ 1 + \left( \frac{2}{g} \right)^2 \left( \frac{1 + \beta}{\beta} \right)^2 \right] \quad (3.13)$$



and for the energy sensitivity

$$\varepsilon_s = \sqrt{\pi} \sqrt{\frac{\beta}{\beta_c}} k_B T \sqrt{LC} \left( 1 + \left(\frac{2}{g}\right)^2 \left(\frac{1+\beta}{\beta}\right)^2 \right). \quad (3.14)$$

By substituting  $g = 2$ ,  $\beta = 1$  and  $\beta_c = 1$  one finds  $\varepsilon_s = 9k_B T \sqrt{LC}$ , which is close to the simulated results. It must be noted that the mixing-down or other excess noise mechanisms have not been taken into account. Eq. (3.14) seems to favor high  $\beta_c$ ; a boundary constraint  $\beta_c \leq 1$  must be applied to avoid multiple modes. In addition,  $g$  is reduced for larger values of  $\beta_c$ .

As a final note on the white noise in SQUIDs, it should be pointed out that the minimum energy resolution given by Eq. (3.12) has a simple physical interpretation [68]. Apart from numerical factors of the order of unity, the minimum energy sensitivity is  $k_B T$  divided by the resonance frequency of the ring, i.e., the thermal energy of the resistors spread uniformly over the bandwidth of the device.

### 3.2.3 Low Frequency Noise

In addition to the white noise discussed above, low-frequency noise is observed in SQUIDs. Its spectral density is characterized by a frequency dependence  $1/f^\alpha$ , where  $\alpha$  is near 1. This flicker or  $1/f$  noise, as it is usually called, is remarkably universal and present in many physical systems. In SQUIDs the suppression of the white-noise levels has made the  $1/f$  noise a very important factor; the corner point where the  $1/f$  noise rises over the white noise level may be several hundred Hertz or even in the kHz range.

In an experimental study by Koch *et al.* [78], the low frequency noise was measured from five different types of tunnel-junction dc SQUIDs. The areas, inductances, and junction capacitances were varied over a substantial range. It was found that the earlier hypothesis of critical current fluctuations [79] due to temperature variations could not explain the observed  $1/f$  noise. The model underestimated the  $1/f$  noise considerably; furthermore, flux and bias-current modulation experiments, where the SQUID could selectively be de-sensitized to critical current differences or to the flux, clearly showed that the noise could be regarded as an apparent *flux* noise. In addition, it was observed that the spectral density was remarkably constant, within a factor of three from  $10^{-10} f^{-1} \Phi_0^2/\text{Hz}$ .

In predicting the low-frequency noise of single junctions the critical current fluctuation hypothesis worked reasonably well, especially for large area junctions [78]. Based on measurements on very small junctions, Rogers and Buhrman [80] showed that conductance fluctuations due to single electron trapping and untrapping in the tunnel barrier could produce the  $1/f$  noise spectrum; later this effect was verified to be effective in a dc SQUID with ultrasmall junctions as well [81].

Recently it has been suggested [82] that the  $1/f$  noise in single junctions and in dc SQUIDs could be due to a thermal feedback effect. In this model, a rise in energy dissipation heats the junction and this correspondingly changes the electrical parameters of the junction, affecting the energy dissipation and closing the cycle. In the dc SQUID, the feedback goes via the flux change introduced by critical current fluctuations: a change in the flux changes the local heating of the junctions, which in turn causes current fluctuations. The authors have compared

their predictions with data previously published, and a good agreement was found. In particular, their theory also reasonably well explains the very low  $1/f$  noise in the SQUIDs by Tesche *et al.* [83] and Foglietti *et al.* [84].

### 3.3 The Coupled dc SQUID

#### 3.3.1 Signal Coupling to the SQUID

SQUID sensors are rarely used by exposing them directly into the field to be measured. Instead, a flux-transformer circuit couples the signal to the SQUID. The device is based on flux conservation in a superconducting circuit; the transformer consists of a pickup coil in the external field and of an input coil inductively coupled to the SQUID. Owing to the external field, a shielding current is induced in the flux transformer, causing, via the input coil, a flux which is applied to the SQUID.

A flux transformer allows the signal to be coupled in a versatile way. Also, the external signal can be collected from a larger volume, increasing the *field* sensitivity, since both the rf and the dc SQUIDs have an energy sensitivity that scales with the inductance of the device and thus with their linear dimensions. In addition, the pickup coil can be configured to reject against uniform fields or its first gradients by adding oppositely wound compensation coils in series. Some flux-transformer pickup-coil configurations are shown in Fig. 3.3.

An elegant alternative way of increasing the effective volume and thus the field sensitivity of a SQUID sensor, without increasing the inductance, is to have

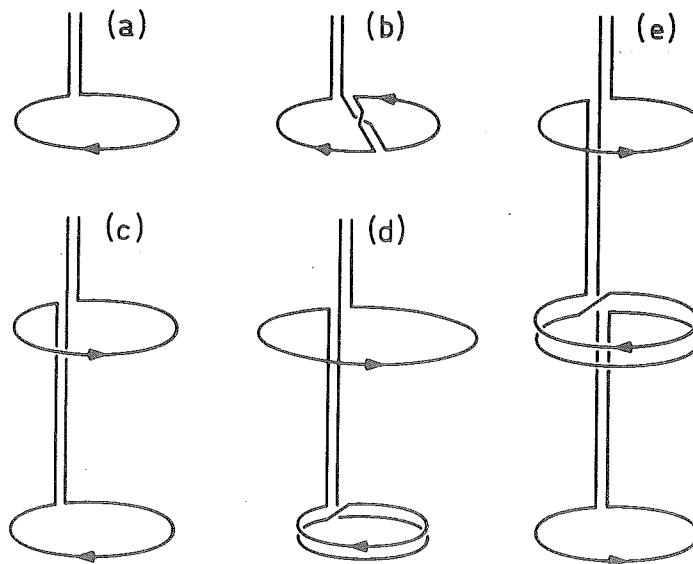


**Figure 3.3.** Configurations of flux transformers. (a) A magnetometer, (b) a first-order off-diagonal gradiometer, (c) a symmetric first-order axial gradiometer, (d) an asymmetric first-order axial gradiometer, and (e) a symmetric second-order axial gradiometer

multiple turns coupled in parallel (the so called fractional-turn SQUID) [85]. This construction is also easily adapted to a gradiometric configuration.

The first SQUIDS were machined out of a bulk superconductor, usually niobium, and the input coil was put in the SQUID hole. In addition to the cylindrical geometry, also a toroidal geometry has been used. The introduction of planar thin-film SQUIDS, although they are in many respects superior to the bulk devices, have posed difficulties in achieving good signal coupling. This problem was solved by Jaycox and Ketchen [86] by integrating the input coil, in planar form, on top of the SQUID. With this technique, coupling coefficients  $k = M/(L_{\text{SQUID}}L_i)^{1/2} > 0.9$  can be achieved, where  $M$  is the mutual inductance between the SQUID and the input coil,  $L_{\text{SQUID}}$  is the SQUID inductance, and  $L_i$  is the input coil inductance.

Their coupling scheme can be modeled with a planar transformer. Assuming that the input coil has  $n$  turns, the inductance  $L_i$  of the input coil can be expressed by [66]

$$L_i = n^2(L_{\text{SQUID}} - L_{\text{par}}) + L_{\text{strip}} \quad (3.15)$$

and the coupling coefficient by

$$k^2 = \left(1 + \frac{L_{\text{strip}}}{(L_{\text{SQUID}} - L_{\text{par}})}\right)^{-1} \left(1 - \frac{L_{\text{par}}}{L_{\text{SQUID}}}\right). \quad (3.16)$$

Here,  $L_{\text{SQUID}}$  is the inductance of the SQUID,  $L_{\text{strip}}$  is the stripline inductance of the secondary over the transformer primary, and  $L_{\text{par}}$  is the parasitic inductance of the transformer primary, mostly associated with the slits of the SQUID loop near the Josephson junctions. The good coupling attainable with the superconducting planar transformer is largely due to the fact that in thin-film structures the ratio of the secondary coil conductor width to the separation between the primary and the secondary can be made large. This reduces parasitic inductances considerably, and almost all the flux is forced through the SQUID ring.

The desire for low noise has lead to very low inductance dc SQUIDS. As a result, inductance matching to practical-sized coils has become a problem. Several solutions to this difficulty have been proposed. The idea of multihole or fractional-turn structures has been applied in thin-film dc SQUIDS [64,87,88], in connection with planar input coils. To achieve better inductance matching, Muhlfelder *et al.* introduced the signal via an extra matching transformer [89]–[91]. Another solution to increase the SQUID area, proposed by Enpuku *et al.* [92]–[95] with simulations and by Ohkawa [96] with a real device, is to release the  $\beta = 1$  constraint and simply allow a big inductance. The problems in SQUID dynamics caused by a large  $\beta$  are then damped by connecting a resistor across the SQUID.

In addition to the planar coupling scheme, integrated planar magnetometers in which the SQUID loop shares a common conductor with a larger field collecting loop have been presented [97]. The resulting signal coupling was poor, however. Later, this structure was modified into a design where the pickup coil is an integral part of the SQUID itself [98]–[102]. Using this technique, very small SQUID inductances cannot, however, be reached. The flux coupling problems and the evolution of integrated magnetometers have been discussed in detail in Refs. [103] and [104].

The advantage of an integrated structure is evident: it allows a compact construction and an excellent dimensional precision for a good intrinsic balance. The

integrated structures discussed above have many problems for optimal design; therefore, the use of a Ketchen-Jaycox type input coil in connection with the pickup coil also made in planar form seems an attractive solution [105]. Quite recently, devices based on this structure have been presented [106]–[107].

### 3.3.2 Effects of Flux-Coupling Circuits on SQUID Operation

The flux-coupling circuits of a practical magnetometer affect the SQUID operation substantially. First, the input coil introduces a parasitic capacitance across the SQUID loop. In particular, with low SQUID inductances, the desire to have a reasonably high input coil inductance for better matching to external coils has led to several tens of turns in the input coil; correspondingly, the parasitic capacitance is high. The effects of this capacitance have been studied by several authors, both with simulations [77,92],[109]–[111] and by means of experiments [88,90,112,113]. In addition to the parasitic capacitance, the input coil also introduces many resonances, as discussed in detail in Publications 9 and 10. Furthermore, the loading of the SQUID by an external circuit can have a significant effect on the performance [77,99,112],[114]–[116].

The noise level of a SQUID suffering from these effects is a sharp function of the applied flux. At some carefully chosen points it may be possible to achieve noise levels comparable to those obtained with a corresponding autonomous SQUID. Attempts to use a practical measurement setup with flux modulation, however, have resulted in a substantially deteriorated performance [91,99,113,117].

So far, the most complete simulations of the coupled SQUID with external circuits, including noise analysis, have been carried out by Seppä and Ryhänen [111]. Their equivalent circuit is shown in Fig. 3.4. It was found that the capacitance and the resonances lead to multiple modes of the SQUID dynamics and to hopping between them; consequently, the low-frequency noise increases. The improvement of the dc SQUID characteristics and the reduction of excess noise by damping the resonance in the input circuit, caused by the capacitance  $C_x$ , was experimentally demonstrated in Publication 9 of this thesis.

The message of the simulations is clear: the parasitic capacitance across the SQUID should be kept well below the junction capacitance and *all* resonances should be properly damped in order to avoid excess noise. The parasitic capacitance  $C_p$  appears as a factor  $(1 + 2C_p/C)\beta_c$  multiplying the second time derivative of the difference phase in the differential equations of the system. Therefore, the effective  $\beta_c$  is increased; a large  $C_p$  thus cancels the advantages of low junction capacitance.

With a multihole structure having perhaps several tens of loops in parallel it is possible to tolerate a large input coil inductance and, with clever design, to avoid large parasitic capacitance. However, the linear dimensions of the structure are relatively large, thus leading to a half-wave transmission line resonance of the SQUID loop which is at a low frequency. This may then easily interfere with the Josephson oscillations at normal points of operation. The same argument applies also to integrated gradiometers which are a part of the SQUID loop. The resistively shunted large- $\beta$  SQUID, in turn, does allow a high output inductance

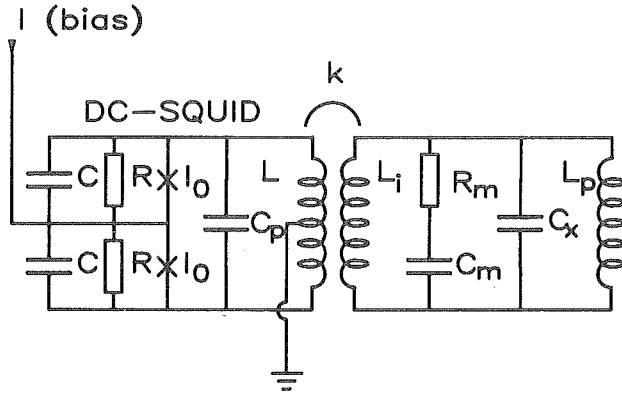


**Figure 3.4.** The equivalent circuit of the coupled SQUID with flux transformer input, after Ref. [111].  $C_p$  denotes the parasitic capacitance across the SQUID, introduced by the input coil, and  $C_x$  is the parasitic capacitance across the flux transformer. The shunt  $C_m$  and  $R_m$  is intentionally added to damp the resonance caused by  $C_x$ .

without an excessive number of turns in the input coil, and the resistor damps the capacitance as well. The price to be paid is the extra noise introduced by the damping resistor and the heavy damping of the junctions, necessary for avoiding excess noise caused by multiple modes.

In the double-loop SQUID construction of Tesche [77,83] the parasitic capacitance is in parallel with an extra capacitance dividing the SQUID loop into two parts. Consequently, at high operating frequencies the SQUID dynamics is affected only by the small loop inductance, shunted by the capacitance across the SQUID. However, at lower operating frequencies multiple modes and excess noise appear since these extra capacitances are not separately damped. This was clearly seen in the measurements of Publication 9, where the noise and flux-voltage characteristics of such a double-loop SQUID were measured as functions of the bias current.

To solve the problems of matching the inductances and to cope with the resonances, the use of an input coil in connection with an intermediate transformer connected to a "normal design" SQUID, with proper precautions, seems to be an attractive alternative. This structure allows enough flexibility to meet the various criteria, which often are counteracting, and it also offers practical advantages, as discussed in Publications 10 and 11.

Because of the transformer, inductance matching and minimization of the parasitic capacitance across the SQUID can be simultaneously fulfilled. In addition, the length of the input coil can be allowed to be longer than the wavelength corresponding to the Josephson oscillations at the average points of operation. Then, the coupling to the SQUID is strongly reduced, and the inductance sensed by the high frequency dynamics remains independent of the external circuits. A change of the apparent inductance towards the unscreened value at high bias currents,

and correspondingly at high frequencies, has also been observed experimentally [112]. Because of this effective decoupling at higher frequencies, the elimination of resonances becomes easier.

### 3.3.3 Optimization of the SQUID Magnetometer

In the past, the SQUID and the flux transformer have been optimized separately. This has lead, for example, to the well-known inductance-matching condition that the sum of inductances of the pickup and compensation coils should equal that of the input coil. As a matter of fact, this does not generally maximize field sensitivity: the condition holds if the input coil inductance can be freely varied and if the coupling between the input coil and the SQUID is independent of the actual values of the inductances. In practice, these conditions are rarely met. Furthermore, one often uses a ready-made SQUID component whose input coil is already fixed, and thus the designer can only change the pickup coil parameters. In this case the equal-inductances condition maximizes the flux input to the SQUID only for tightly wound coils, which are rarely desirable in practical magnetometers [118]. Even if the designer can choose the SQUID parameters, the coupling coefficient is not completely independent of the inductances.

The design of the flux transformer and the SQUID should not be separated, but the system should rather be optimized as a unit where the various interrelationships are taken into account. As discussed in the previous section, the interaction between the SQUID and the external circuits becomes particularly important in thin-film integrated structures.

Unfortunately, writing down the differential equations of the whole system with external circuits and parasitic elements and then optimizing the design numerically is far too tedious. Even the calculation of the behavior of the system with specific values of the parameters requires vast amounts of computing, let alone scanning the parameter space for optimum. For optimizing, a simplified model for the system has to be developed. A solution to this problem is to use a modified autonomous SQUID model as a building block, since it has already been thoroughly studied. To apply this type of approach it must be required, of course, that the high-frequency dynamics of the SQUID is not much perturbed by the external circuits, i.e., the system is free from multiple-mode solutions and hopping between modes. Then, suitable interrelationships can be developed between the external circuit and the SQUID parameters and the sensitivity of the magnetometer. Also, constraints and dependencies caused by the fabrication technology have to be taken into account in the model.

The above mentioned questions have been discussed in detail in Publication 10, where we present the design and construction of a dc SQUID to be connected to a pickup coil via an intermediate transformer. As a result of minimization of the capacitance across the SQUID, signal decoupling at high frequencies, and proper damping of the resonances, the use of the autonomous SQUID model as a basis for the optimization is well established. In the sensitivity calculations the geometry was built in: the actual dimensions were the variables to be optimized. This allowed the inclusion of fabrication-dependent constraints and interrelationships of parameters, e.g. the dependence of coupling coefficients on the inductances.

The resulting SQUIDs showed smooth characteristics and low noise. In the best samples, the noise level,  $1.3 \times 10^{-6} \Phi_0/\sqrt{\text{Hz}}$ , is comparable to that of calculations where only the noise from the junction shunt resistors was included, showing that our SQUIDs do not suffer from excess noise processes, thus experimentally verifying the basic design principles.

### 3.4 Signal Readout and Electronics for the dc SQUID

With SQUID sensors, at least in neuromagnetic research, one is usually interested in measuring signals whose frequency content is below a few kHz. For these low-frequency signals, the SQUID offers unrivaled sensitivity. Semiconductor preamplifiers used to read out the SQUID signal, however, operate best at higher frequencies, starting from several tens of kHz. To avoid drifts and to make use of the minimum noise, the SQUID signal is normally read out with a flux modulation technique, operating at a frequency of the order of 100 kHz. Converting the quasi-dc signal to higher frequencies also allows the use of passive impedance matching elements for improving the signal-to-noise ratio.

In the flux modulation scheme, a square-wave flux of amplitude  $\Phi_0/2$  is superimposed on the input flux, and the signal is detected phase-sensitively. As seen from Figs. 3.5a and b, the output component at the modulation frequency is zero at input flux values of  $n\Phi_0/2$ , where  $n$  is an integer, and at a maximum when the input flux equals  $(2n + 1)\Phi_0/4$ . In the flux-locked-loop operation, the detected signal is fed back to the SQUID to keep the output of the detector zero and thus to lock the operating point. This way, the periodic response of the SQUID is linearized over a wide range of the variation of the input flux.

A block diagram of the electronics is shown in Fig. 3.5c. Phase-sensitive detecting (PSD) is usually accomplished by multiplying with a square-wave reference signal. Its phase, with respect to the modulating signal, can be adjusted to compensate for phase shifts in the preamplifier. The modulating frequency and its harmonics are removed by low-pass filtering or by integrating over a half-period of the modulation cycle. After that, the detected signal is brought to a proportional-plus-integral controller (PI) [119] whose output is then fed back to the SQUID. The PI-controller gives an output proportional to the input plus its time integral; the effect is to keep the output of the detector zero. The readout and operation of the SQUID in a feedback loop have been discussed in detail, for example, in the review by Giffard [120].

If there is high-frequency noise in the input of the SQUID, a fraction of it is seen in the output because of mixing down in the detector. For white-noise input and a preamplifier bandpass around the modulation frequency, this mixed-down contribution has been calculated in Publication 9.

The dc SQUID is usually connected to the preamplifier via an impedance matching transformer. If the voltage noise of the preamplifier is  $e_n$  and the current noise is  $i_n$ , the signal-to-noise ratio is maximized when the impedance seen by the preamplifier equals  $e_n/i_n$  [121,122]. In a typical FET preamplifier this optimum source impedance is of the order of kilo-ohms, whereas the output impedance of the

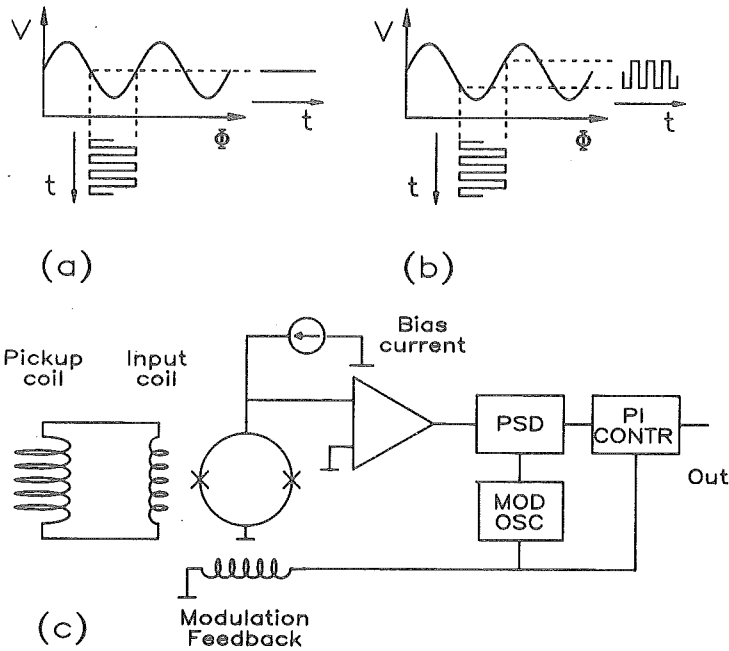


Figure 3.5. Schematic view of the flux modulation and feedback. (a) Input flux  $\Phi_0/2$ , no output at the modulation frequency. (b) Input flux slightly offset from (a): output at the modulation frequency appears. (c) Block diagram of the SQUID electronics. Details are described in the text.

dc SQUID, its dynamic resistance, is only a few ohms. To achieve this impedance step-up, usually a series resonant  $LC$  circuit is used. However, the  $Q$  value of such a circuit has to be rather large, limiting the available bandwidth; by using a transformer instead of the  $LC$  circuit, the bandwidth can be increased. The noise contribution of the preamplifier, with proper impedance matching, can be kept negligibly small compared with the noise of the SQUID; for example, the noise temperature of our preamplifier described in Publication 4 was 2 K.



## 4 Multichannel Neuromagnetometers

### 4.1 The State of the Art

Until recently, all neuromagnetic measurements were carried out using single-channel magnetometers or gradiometers, with their pickup and compensation coils wound of superconducting wire on three-dimensional formers. The optimization of the coil parameters, i.e. the coil diameter and length, the number of turns, and the baseline of the gradiometer, for good sensitivity and good discrimination against external disturbances has been discussed by several authors [123]–[127]. Besides maximizing the field sensitivity, the field distribution of the biomagnetic signal and of the disturbances have to be taken into consideration in designing an optimal gradiometer coil configuration. For example, enlarging the coil diameter increases sensitivity but reduces spatial resolution. Some general rules of thumb can be stated, e.g., the coil diameter should not be greater than the average distance to the source [123,127], and the baseline should be chosen 1 – 2 times the distance to the source [124,126]. The coil parameter design has been discussed in detail also in Publication 4.

The double-D gradiometer of Cohen [128] was the first multichannel instrument put into use. It consisted of two mutually orthogonal off-diagonal gradiometers, shown schematically in Fig. 3.3b, measuring the components  $\partial B_z/\partial x$  and  $\partial B_z/\partial y$ . The diameter of the coils was 2.8 cm, and the gradient sensitivity of the 2-D detectors was  $1.6 \text{ pT}/(\text{m} \cdot \sqrt{\text{Hz}})$ .

For localization of neuromagnetic sources, a multichannel SQUID magnetometers measuring the field at several locations simultaneously was first used by Ilmoniemi *et al.* [118]. Their 4-channel first-order gradiometer consisted of three ellipsoidal pickup coils inside a 30-mm circle and a fourth circular 21-mm-diameter coil 12 mm above the lower coils; the field sensitivities of this rf-SQUID instrument were 22 and  $15 \text{ fT}/\sqrt{\text{Hz}}$  in the lower and upper coils, respectively.

A 5-channel dc-SQUID system was later installed in New York [129] and a 4-channel rf-SQUID system in Rome [130]. Both devices, utilizing second-order gradiometers, were designed for use in an unshielded environment; their 15-mm diameter pickup coils were located inside circles of 55 and 45 mm in diameter. The noise levels quoted were 20 and  $50 \text{ fT}/\sqrt{\text{Hz}}$ , respectively.

At present, a 7-channel second-order gradiometer is commercially available [131]. The coils used in this device are similar to those used in the New York 5-channel device, having symmetrical compensation coils and a 4-cm baseline; the seven coils are located inside a 55-mm-diameter circle. Several units, including also two-dewar  $2 \times 7$ -channel systems have been or are currently being installed.

In this thesis, the detailed design, optimization, and construction of a low-noise 7-channel first-order dc SQUID gradiometer will be described (Publication 4). The device, shown schematically in Fig. 4.1, covers a spherical cap area of

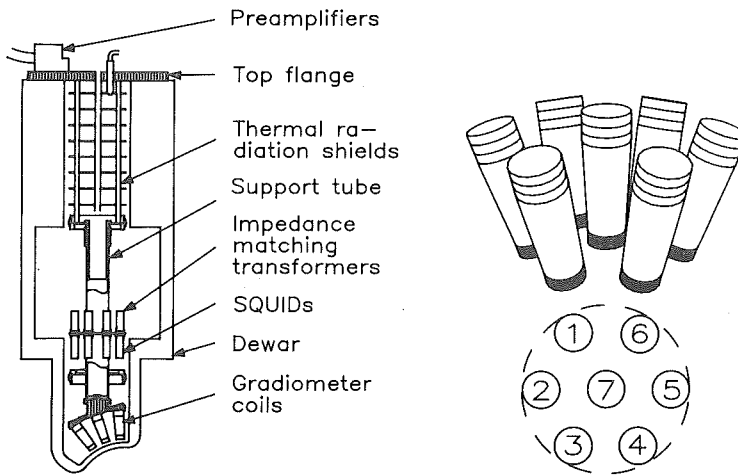


**Figure 4.1.** The mechanical construction and coil configuration of our seven-channel gradiometer.

**TABLE I.** Comparison of Multichannel Magnetometers

	Ilmoniemi <i>et al.</i> [118]	Williamson <i>et al.</i> [129]	Romani <i>et al.</i> [130]	BTi [131]	Publication 4
Channels	4	5	4	7	7
Pickup diam. [mm]	20/12 <sup>1</sup> , 21 <sup>2</sup>	15	15	15	20
Gradiometer order	1	2	2	2	1
Baseline [mm]	60	40	53	40	60
Channel sep. [mm]	16 <sup>3</sup>	20	21	20	36.5
Noise [fT/√Hz]	22 <sup>4</sup> , 15 <sup>5</sup>	20	50	20	5

<sup>1</sup>Ellipsoid axes of the lower coils

<sup>2</sup>Diameter of the upper circular coil

<sup>3</sup>Distance between the centers of the coils, located at the vertices of a regular tetrahedron

<sup>4</sup>Lower coils

<sup>5</sup>Upper coils

93 mm in diameter; the sphere radius is 125 mm. The sensitivity of the channels is  $5 \text{ fT}/\sqrt{\text{Hz}}$ , mainly limited by the thermal noise from radiation shields of the dewar, and the  $1/f$  is very low with the corner point at a few tenths of Hertz.

The key parameters of the above mentioned multichannel magnetometers have been summarized in Table I. The noise levels reported in the table depend, of course, on the particular installation and on the testing conditions.

In addition to these multi-SQUID instruments, vector magnetometers measuring all three field components at one point have been introduced [132]–[134]. All these devices use three rf SQUIDs but in the readout multiplexing of the three

channels is applied in Refs. [132] and [134], using frequency or time division.

At present, seven channels in a hexagonal grid seems to be the *de facto* standard for MEG instrumentation; most of the devices are second-order gradiometers. Magnetically shielded rooms are also being built in several laboratories; mu-metal rooms are now commercially available.

The 7-channel instruments are obviously only one step toward magnetometers with still more channels, covering the whole area of interest in one measurement. Only then routine clinical studies become feasible. Several plans of devices having 20 – 30 or even 100 SQUIDs have been put forward. However, the construction of multiple-SQUID systems is not just multiplication of previous designs; many new problems are introduced [10].

The use of 20 – 30 conventional, wire-wound axial gradiometers leads to a bulky, elaborate, and expensive construction. In addition, the conical space required by axial gradiometers may lead to space problems in dewar design. Axial gradiometers, measuring the radial component of the field, have been popular because of the easy intuitive interpretation of the results. Since the baselines are usually longer than the distance to the sources, the signal measured by the gradiometer is well approximated by the field at the pickup coil; the effect of compensation coils is merely to cancel uniform fields. However, other components and derivatives are, in principle, not more difficult to analyze and should thus not be rejected *a priori*. With magnetometers the difficulties in construction would be simpler and there would be no problems in the interpretation of data; in practice, however, the use of magnetometers is not usually feasible, even inside magnetically shielded rooms, because of vibrations of the dewar in the remanent magnetic field and because of other nearby noise sources, e.g., the heart of the subject.

To avoid problems of wire-wound gradiometers in multichannel devices, there has been a growing interest for planar integrated sensors [10,135,136]. Practical and experimental planar gradiometer and magnetometer components for neuro-magnetic use have been presented quite recently (Publication 11, Refs [107],[108]).

The structure of our integrated sensor, described in Publication 11, is shown schematically in Fig. 4.2. It consists of two orthogonal figure-of-eight shaped off-diagonal gradiometers, measuring  $\partial B_z/\partial x$  and  $\partial B_z/\partial y$ . The overall pickup coil size is  $28 \times 28 \text{ mm}^2$ . The signals are coupled to two dc SQUIDs, located on separate  $6 \times 9 \text{ mm}^2$  chips, via intermediate transformers. All the three chips are glued together and mounted on a fiber glass holder to form a single component. This separate-chip construction, possible without superconducting contacts thanks to the transformer, allows flexibility in use since to change the pickup coil design it is not necessary to redesign the whole SQUID. The intermediate transformer and the SQUID have two oppositely wound coils to avoid spurious signals due to homogeneous fields. The gradient sensitivity of this sensor is better than  $450 \text{ fT}/(\text{m} \cdot \sqrt{\text{Hz}})$ ; however, due to difficulties in fabrication, the yield has been low, so far.

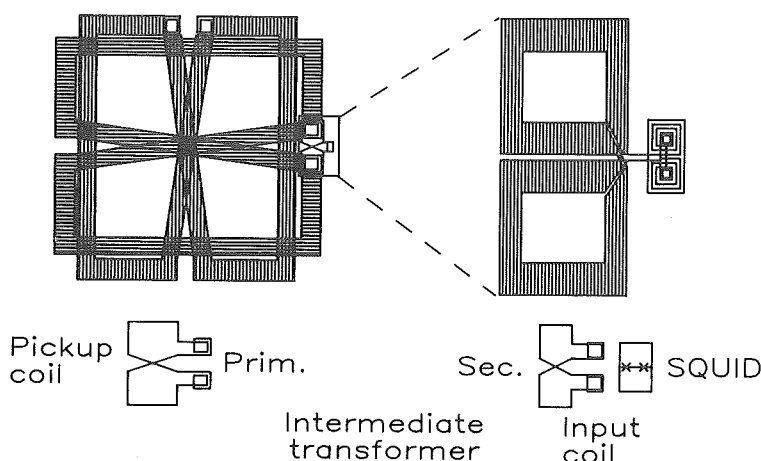


**Figure 4.2.** Schematic structure of the integrated SQUID gradiometer described in this thesis. See text for details.

## 4.2 Design and Construction of Multichannel Magnetometers

### 4.2.1 Design Criteria

A major goal in magnetoencephalographic studies is to locate cortical sources. Therefore, one of the principal criteria for an optimal design of multichannel magnetometers should be the spatial resolution which is affected both by the sensitivity and by the distribution of the sensors, making it a suitable figure-of-merit with a clear connection to practice. For locating accuracy calculations, some characteristics of the signal to be measured must be known in advance. This method was applied in the design of our 7-channel gradiometer; for further discussion, see Publication 4.

The optimal distribution of sensors may also be considered from a different point of view. If the spatial frequency content of the signal to be measured is known, the spatial analog of the Nyquist sampling theory can be applied to determine a suitable spacing for the measurement grid [137]. For a typical field distribution caused by current dipoles, for example, the maximum spatial frequency varies, depending on the depth of the source, between 10 and 30  $\text{m}^{-1}$ . Thus, a suitable grid spacing is of the order of 20 – 30 mm. In addition, to apply this criterion, a sufficiently large area of coverage must be assumed. In the 7-channel magnetometer, where the number of the channels was fixed in advance, and the area of coverage was determined by the grid spacing, the optimum, 36.5 mm, turned out to be larger than predicted by simple spatial-frequency analysis. With a fixed number of channels, it is also instructive to calculate the angles between the lead fields of the channels, as discussed in Publications 2 and 4. This angle is

a measure of the amount of *different* information conveyed by the channels.

#### 4.2.2 Planar Gradiometer Arrays

As mentioned before, the use of off-diagonal derivatives measured by planar gradiometers does not, in principle, reduce the spatial resolution. To test the feasibility of off-diagonal gradiometers, the errors in locating cortical current dipoles have been numerically simulated for planar arrays in Publication 3 and in Refs. [135] and [136]. We found that the locating accuracy of first-order planar gradiometers is essentially the same as for axial first-order gradiometers; the higher-order gradiometers investigated in Refs. [135,136] were in some cases more advantageous than second-order axial gradiometers. The advantage of planar gradiometers seems to be in their better sensitivity for small differences in the field, like the orientation of the sources, for example. This is due to the non-rotational symmetry of the sensors.

The “field patterns” measured by off-diagonal gradiometers are, of course, morphologically different from those of axial gradiometers. For example, the first-order gradiometer, like the 2-D [128], gives the maximum response directly over the source, with the direction of the current perpendicular to the direction of the gradient. This is demonstrated in Fig. 4.3 for a current dipole. It is seen that the maximum response is well localized, the 50 % width of the peak being 35 – 55 mm for dipoles 20 – 40 mm below the scalp. The corresponding spatial frequencies, at which the amplitudes of the spectral components have dropped under 10 %, are 20 and 30  $\text{m}^{-1}$ , respectively. Thus, it is seen that the size of the sensors should be

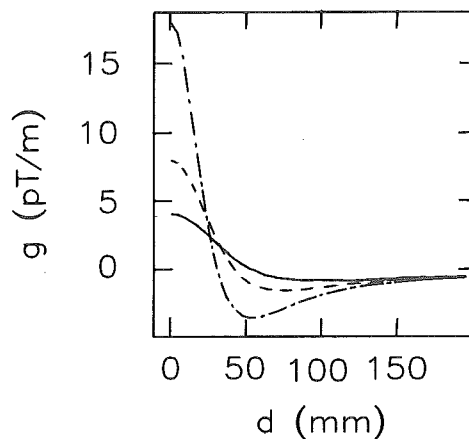


**Figure 4.3.** The off-diagonal gradient  $\partial B_z / \partial x$  of a 10-nAm dipole in the direction perpendicular to the dipole, on the surface of a sphere with a 125 mm radius. The distance from the gradiometer to the surface of the head was 15 mm, and the depth of the dipole was 40 (solid line), 30 (dashed line), and 20 mm (dash-dotted line) below scalp. The horizontal axis reads the distance along the surface of the sphere from the line above the dipole.

less than 30 mm, and that a grid spacing of 20 – 30 mm, for example, does not cause severe aliasing.

### 4.2.3 Practical Aspects

The design of the sensor configuration must meet several practical constraints, such as the dewar space available and avoiding of a too complicated and bulky construction. The materials have to be carefully chosen; for example, careless cabling to SQUIDS can increase the liquid helium boiloff rate to an intolerable level since, for a 30-channel dc SQUID system, 90 cables are needed if no special techniques are used in wiring.

In the design, compact modular construction should be preferred whenever possible. This is especially important in the construction of the electronics: it has to be kept simple, easily-operated, and compact. When many channels are simultaneously used, the possibility of computer control is an important feature. Furthermore, to avoid cross talk between the channels, cables have to be well shielded or carefully symmetrized; this is also important for noise immunity of the system. For very high sensitivity magnetometers, proper grounding arrangements are essential.

Making dewars for wide-area multichannel magnetometers causes several problems, too. The larger the area, the more difficult it is to fit the curved bottom closely to the head. Because of considerable interindividual variations, a tight-fitting, head-shaped dewar bottom is impossible to make; one may use a spherical bottom to approximate the local radius of curvature, but then the maximum area is obviously limited. The fact that some of the channels may be rather far from the surface of the head naturally puts high demands on the sensitivity of the SQUIDS. In addition, a wide sensing area implies a rather large gap between the room temperature surface and the 4.2-K interior.

## 4.3 Use of Multichannel Magnetometers

### 4.3.1 Calibration and Dewar Position Indication

Because the flux transformers form superconducting loops, the field around the coils is distorted due to shielding currents. As a result, the channels in a multichannel magnetometer do not measure the true field. If the mutual inductances between the channels are known, the correction is easily calculated. Assume that there are  $n$  channels and that the mutual inductances are described by the  $n \times n$  matrix  $M$ . Let further  $\Phi' = (\Phi'_1 \dots \Phi'_n)^T$  be the net fluxes measured by the flux transformers and  $\Phi$  the undistorted applied flux. Then,

$$\Phi = (I - L^{-1}M)\Phi', \quad (4.1)$$

where  $L = \text{diag}(L_1 \dots L_n)$  is a diagonal matrix containing the total inductances of the flux transformers and  $I$  is the identity matrix.

In practice, one measures the output voltages  $V = (V_1 \dots V_n)^T$ , which are related to the measured fluxes  $\Phi'$  via calibration coefficients  $K_1 \dots K_n$ . Normally,

these coefficients have to be measured *in situ* with all the channels. Since in MEG measurements the field distribution generally differs from that used in the calibration, the effects of coupling also differ. Consequently, the calibrations  $K_i$  cannot be simply calculated from  $\Phi_i/V_i$ , where now the applied flux  $\Phi$  is calculated from the geometry of the experimental setup. Instead, the *true* calibration  $\Phi_i'/V_i$  is obtained by inverting Eq. (4.1).

As there are  $n(n-1)/2$  independent mutual inductances between  $n$  channels, the number of parameters is large. Fortunately, often only the nearest neighbors need to be taken into account, which substantially reduces the number of parameters. The situation becomes complicated if the mutual inductances cannot be measured directly. The best way is then to calibrate the device with a phantom whose field distribution closely resembles that generated by the brain, thus taking the interchannel interference corrections into account in the calibration coefficients.

An elegant alternative solution to the above-mentioned problems has been presented by ter Brake *et al.* [138]. In their method, flux feedback is applied to the flux transformer rather than directly to the SQUID, as in the conventional technique. Now, the feedback keeps the flux transformer effectively currentless, thus eliminating the cross talk between channels.

Large dewars are in practice more difficult to position accurately with respect to the head than small ones. Thus, an automatic system to indicate the location and orientation of the magnetometer is of great importance. The positioning problem is especially severe with the present instruments where mechanical scanning over the head is needed. The uncertainty in the position and orientation of the magnetometer can be considered as an extra source of noise [130]. Location indicators based on magnetic determination of the dewar position have been constructed to overcome this problem. One possible solution is described in Publication 4. In this method, a set of three test coils is attached on the head and then the signal due to these coils is measured with the SQUIDs; the test coil positions with respect to the magnetometer are then found by a least-squares search. Another solution [131] uses three orthogonal coils in the receiver and in the transmitter; from the measured signals of a few such transmitters the position and the orientation of the magnetometer can be found.

### 4.3.2 Correlated Noise

During evoked-response measurements, the simultaneous background activity of the brain also adds to the recorded signals. If this background is not relevant to the experiment, it can be considered noise. This subject noise, however, ultimately limits the signal-to-noise ratio in experiments made with the best SQUID magnetometers. In contrast to the uncorrelated instrumental noise, the subject noise is, however, correlated in the simultaneously measuring channels. The correlation can, in principle, be taken into account in the signal analysis to reduce the effect of subject noise.

In Publication 5, spatial and spectral characteristics of subject noise have been measured. The spectral density,  $S_i^{1/2}$ , of the subject noise is typically 20 – 40 fT/ $\sqrt{\text{Hz}}$  below about 20 Hz, decreasing towards higher frequencies. Therefore, at these low frequencies, contribution of instrumental noise is negligible. Since the

subject noise is often not time-locked to the stimulus, its effect can, of course, be reduced by signal averaging. The normalized coherence functions show substantial correlation even in channels located 73 mm apart; in frequency the correlation extends up to 50 – 60 Hz.

The observed long-range correlation has important practical consequences for the analysis of evoked responses. Multiple, simultaneously measured data can be used to estimate the covariance matrix  $\Sigma$  for the field errors at different sites. This matrix can then be inserted to the least-squares search of the equivalent current dipole in the way described in Section 1.3. Its effect is to reduce the variance of the maximum likelihood estimate, which can be described by the change in the volume of the 5-dimensional hyperellipsoid, given by Eq. (1.6). In Publication 5, an example is calculated; we show that this reduction is significant, demonstrating the advantages of simultaneously measured multiple recordings in obtaining more accurate estimates for the source parameters.

### 4.3.3 Examples of MEG Measurements

A demonstration of the capabilities of very sensitive multichannel measurements is provided by the study of the middle-latency (about 30 – 60 ms after the stimulus onset) components in the auditory evoked response following short noise bursts [139], carried out using the 7-channel magnetometer described in this thesis. These components are very weak, only 40 – 50 fT, which puts high demands on the instrumentation. The origin of the 30-ms component has been controversial on the basis of earlier experiments; both subcortical and cortical sources have been suggested. The successful field mapping (see Fig. 4.4) indicated that the 30-ms component originates at the auditory cortex, slightly anterior to the main auditory response at 100 ms after the stimulus onset.

The alpha-activity of the brain, present in a relaxed subject having his eyes closed, produces a strong (1 – 2 pT) spontaneous signal at a frequency of approximately 10 Hz. An example of the alpha rhythm is given in Fig. 4.5. Locating the sources of this activity has been difficult using only single-channel instruments because of the ever-varying nature of the oscillations. Special techniques, employing the simultaneously measured EEG as a reference, have been developed [140], leading to a model of two alpha generator dipoles, one at each hemisphere. Real-time locating of the sources is, of course, possible only when one is able to cover a large portion of the head simultaneously. At present, when multichannel instruments are being established in several laboratories, new experiments on spontaneous activity are expected to emerge.



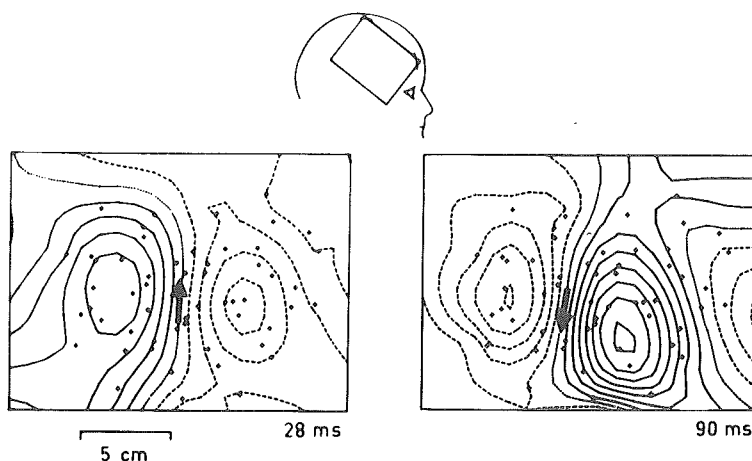


**Figure 4.4.** Field maps on one subject over the right hemisphere at 28 ms and 90 ms after the onset of the noise burst stimulus. Solid lines indicate flux out of the skull and dashed lines flux into the head; the contours are separated by 10 fT. Dots indicate the midpoints of individual channels. The estimated positions of the equivalent dipoles are shown by arrows. Modified from Ref. [139].

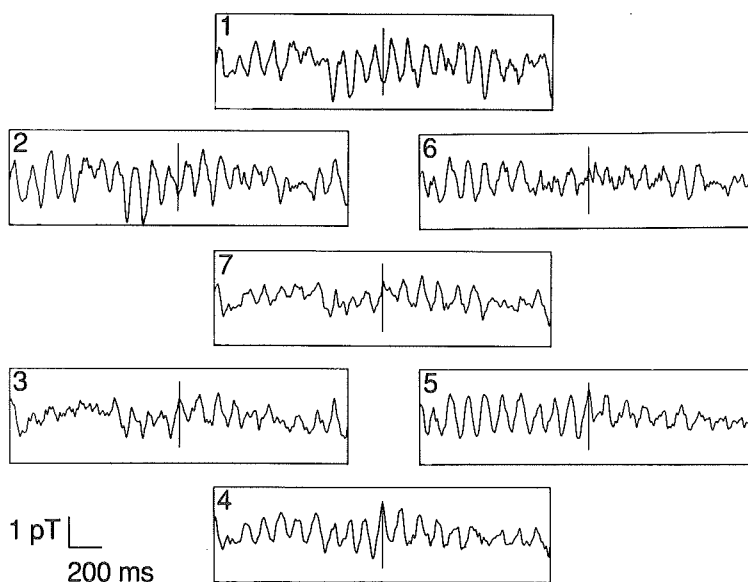


**Figure 4.5.** An example of the alpha rhythm, recorded over the occipital lobe of a subject having his eyes closed. The traces were measured using our 7-channel magnetometer; the bandwidth was 0.05 – 50 Hz. Note the polarity reversal between, for example, Channels 1 and 4 at the time instant marked with a vertical bar.

## 5 Discussion

### 5.1 New Superconductor Materials

In 1986 – 1987, the discovery of new superconducting ceramic oxide compounds started a spectacular period in solid state physics. After the first evidence of superconductivity in rare earth - copper oxides at temperatures higher than in conventional superconducting materials [141], the research activity has rapidly expanded, leading to an unseen speed of progress. Materials with a critical temperature of over 90 K [142] have been well established; signs for the onset of superconductivity have been announced near room temperature, but in all cases the sample properties are either unstable or the results are not confirmed. This enthusiasm is attributable not only to the scientific interest but also to the large potential for applications of high-temperature superconductors.

However, in spite of the large research effort the picture on the new materials is still far from being complete; for example, the theoretical foundation of superconductivity in these new materials is not clear, although many suggestions have been made. The number of publications on high- $T_c$  superconductors is already very large and rapidly growing; for a recent survey of experimental and theoretical phenomena see, for example, the Proceedings of the 18th Low Temperature Physics Conference [143].

The two main groups of materials investigated have been the Yttrium-Barium-Copper-Oxide and Lanthanum-Barium-Copper-Oxide compounds. Most samples of these ceramic materials have been small pellets of randomly oriented crystals; for any practical applications, however, it is of vital importance to be able to make high-quality wires or thin films. The unfavorable mechanical, chemical, crystalline, and physical properties of the materials complicate this task substantially. For example, during the deposition the film reacts with many substrates and, furthermore, the patterning of the film may substantially affect its properties. In addition, the materials are highly anisotropic, and grain boundaries which can act as Josephson junctions are easily formed. This may lead to very small critical current densities in certain directions.

The Josephson effect has also been observed in these high- $T_c$  materials [144]–[148]. In most of the studies, microbridge-type junctions have been used; very little data exist on SIS-type junctions. The microbridges, however, have been larger than the estimated coherence length, suggesting that the junctions probably form between grain boundaries.

SQUIDS made of these materials have been reported by several laboratories: dc SQUID operation was demonstrated by the groups at IBM [149], Hitachi Corporation [150], and Tsukuba University [151]; rf SQUIDS have been constructed by the NBS [152], University of Strathclyde [153], and Wihuri Research Institute [154] groups. So far, the devices have merely been used to experimentally demonstrate

the Josephson and the quantum interference effects in high- $T_c$  superconductors. Furthermore, only the IBM and Hitachi SQUIDs were made from thin films. The lowest reported noise so far, with the SQUID operated in liquid nitrogen at 77 K and using flux modulation, has been  $4.5 \times 10^{-4} \Phi_0/\sqrt{\text{Hz}}$  in the NBS SQUID [152].

The possibility of operating SQUIDs in liquid nitrogen or possibly at even higher temperatures may become important for neuromagnetic instrumentation. The new devices could operate without liquid helium, which has been one of the main drawbacks attributed to work with SQUIDs. Since the noise of the SQUID scales with the operating temperature, the key question is what will be the attainable sensitivity, and whether it will be sufficient for neuromagnetic research.

At high temperatures, the inductance of dc SQUIDs has to be rather small, only some tens of pH; this is seen by requiring that the noise rounding parameter  $\Gamma = 2\pi k_B T / \Phi_0 I_0$  be sufficiently small and that  $\beta \simeq 1$  [149]. This, of course, poses high demands on the geometrical design, including signal coupling and the minimization of parasitic inductances. With proper optimization and assuming no extra noise sources, however, noise levels of the order of  $10^{-5} \Phi_0/\sqrt{\text{Hz}}$  should be possible at liquid nitrogen temperatures; the corresponding energy sensitivity is then  $10^{-30} \dots 10^{-29}$  Js.

For many purposes this is clearly sufficient, and it may even be enough for neuromagnetometers with wire-wound flux transformers. However, in constructing small integrated devices there is, even with modern 4.2-K SQUIDs not much sensitivity to spare; high-temperature SQUIDs may be too insensitive for MEG.

With high- $T_c$  materials it may be possible to get the sensors closer to the head, increasing the signal amplitude significantly. A good combination of high sensitivity and close to the head sensors could be obtained by a hybrid structure, with a high- $T_c$  pickup coil and a 4.2 K SQUID. The cost of liquid He for this solution is, at least in laboratory environment, not a limiting factor.

A further aspect of the new materials may be noted. The rise in the operating temperature makes the use of closed-cycle refrigerators a more attractive solution. If small, cheap, and vibration-isolated cryocoolers become available, it is possible to eliminate the need for liquid helium and, simultaneously, have a sensitivity not substantially worse than that obtained by operating the SQUID at 4.2 K.

In conclusion, it is too early to judge the real significance of the new oxide superconductors. The aspects discussed here are just speculations on how they might affect neuromagnetic research; for practical demonstrations, much research must still be done.

## 5.2 Clinical Applications

During the last years, several new medical imaging techniques have been introduced in clinical brain diagnostics, including computerized X-ray tomography (CT scan), nuclear magnetic resonance (NMR) imaging, positron emission tomography (PET), and cerebral blood flow (CBF) monitoring. The results obtained with these methods have been quite impressive, allowing for better noninvasive diagnosis. The CT scan and NMR imaging give *anatomical* information; many disorders are, however, not associated with a clear lesion or change in the gross anatomical

structure. Therefore, *functional* localization is often needed. PET and CBF are both based on changes in metabolic activity; correspondingly, the time resolution is rather poor. Both EEG and MEG, the only noninvasive methods probing the electric activity of the brain directly, can provide a millisecond time resolution. Furthermore, both techniques are completely harmless since the subject is not exposed to X-rays, strong magnetic fields or internally delivered radioactive tracers. As discussed previously, the spatial resolution of MEG is, however, superior to EEG.

MEG will, of course, not replace any of the abovementioned methods but provide complementary information. So far, the most promising clinical application of magnetoencephalographic measurements is the locating of epileptic foci. Besides for diagnostic purposes, accurate localization is needed if surgical operations are planned. MEG can provide substantially better spatial resolution than electric scalp measurements without the risks of invasive intracranial recordings.

Most of the experiments, being carried out with single-channel devices, have relied on the simultaneous use of EEG as a reference [155,156]; the experimental problems are analogous to those in the studies of other spontaneous brain activity. For routine clinical measurements, a device which covers the whole area of interest is of course a necessity.

In the future, with a good clinical multichannel MEG system, it might even become feasible to replace some of the routine EEG measurements, since in MEG no leads have to be attached to the patient which makes faster measurements possible. With more clinical data, medical applications in which the better locating power of MEG substantially helps in the diagnosis may well be discovered, leading to further expansion in hospital use.

At present, there are several barriers to be removed for routine clinical applications. The main technological problem so far has been the lack of a sufficient number of channels; the long time required for measurements has effectively limited the studies to a small experimental scale. In the next few years, this problem will be largely solved by the new-generation instruments.

The need for effective and expensive shielding will remain one of the main disadvantages of MEG. The shield constitutes a major part of the total cost, although the price of a complete MEG setup is considerably less than that of a high-field NMR imaging system, for example. Experience has shown that mu-metal shielding is really necessary; the use of high-order gradiometers reduces the sensitivity too much and electronic active noise cancellation schemes suffer from limited dynamic range and from the complex tuning procedure required. Trying to make the shielding cheaper is thus important; a further unanswered question is whether superconducting shields made from the new oxide materials could be utilized.

Furthermore, even despite of shielding, the MEG laboratory should preferably be located in special rooms in a magnetically clean environment sufficiently far from other instrumentation. In many hospitals, this may be difficult to realize without investing to new buildings.

Liquid helium has also been one of the main drawbacks of a SQUID system. The running costs can be cut down quite effectively by a boiloff gas collecting system; the regular refilling of the dewar, necessary 2 – 3 times a week in present

systems, is a considerable inconvenience in a hospital environment. Longer refilling periods are very difficult to achieve without making the dewars extremely massive and difficult to handle; here, too, the future development of new superconductor materials and efficient cryocoolers may provide a substantial improvement to this problem.

So far, all the devices have been intended for laboratory use by highly trained personnel. For routine clinical studies, easy-to-use and reliable instruments with minimal required maintenance are needed. The SQUID magnetometers are rather delicate instruments, susceptible to all kinds of disturbances. Thus, a considerable research and development work must be carried out in going from laboratory prototypes to practical devices. Also, the user interface via a computer with all its data analysis software requires another very large effort.

### 5.3 Conclusions

The development of the SQUIDs has come to the point where little further progress in reducing the minimum noise is to be expected. Experimental SQUIDs have been demonstrated to reach energy sensitivities of one Planck's constant. Owing to the reduction of excess noise, practical SQUIDs, with flux coupling circuits, have approached theoretically predicted white noise levels. Experimental evidence and gradually increasing understanding of the low-frequency noise mechanisms have shown that the feared  $1/f$  noise can also be kept at a sufficiently low level. These facts, together with better junction fabrication techniques, provide practical sensors with high sensitivity, well-behaved characteristics, and stable operation. For applications, the main emphasis is on building a cheap and reliable SQUID component; higher operating temperatures may also prove to be one of the main directions for the future development.

At present, we are living in a period of change: the present few-channel magnetometers will be replaced in a few years by units with several tens of SQUIDs. These new-generation instruments will have a major impact on neuromagnetism. Faster data collection, provided by the possibility to record the whole field pattern without moving the instrument, enables more complicated experiments and studies of patients, and improves the reliability of results.

The full utilization of multichannel magnetometers is, however, only taking its first steps. The massive stream of information coming from such magnetometers requires good data processing capability, with perhaps data compression. Also, the form of viewing the data, whether consisting of, e.g., off-diagonal gradients or actual magnetic fields, should be reconsidered. It has to be borne in mind that the magnetic field *per se* is only a means of obtaining an estimate of the actual goal, the current distribution. Furthermore, the coherent noise should be effectively taken into account in the analysis to take full advantage of the high sensitivities available with present magnetometers. Therefore, in addition to technical development of instruments, new ways of thinking are needed in the signal analysis and in the inverse problem studies to extract the maximum amount of information from the simultaneously measured signals.

## 6 Contents of the Thesis

### 6.1 List of Publications

This thesis consists of the following publications:

1. M.S. Hämäläinen, R.J. Ilmoniemi, J. Knuutila, and K. Reinikainen, "Analysis of Magnetoencephalographic Data Obtained with a Four-Channel SQUID Magnetometer", in: *Biomagnetism: Applications & Theory*, eds. H. Weinberg, G. Stroink, and T. Katila. (Pergamon Press, New York, 1985), pp. 299 – 303.
2. R. Ilmoniemi and J. Knuutila, "Remarks on the Design of a Four-Channel SQUID Magnetometer for Brain Research", in: *Proceedings of the Tenth International Cryogenic Engineering Conference ICEC10*, eds. H. Collan, P. Berglund, and M. Krusius. (Butterworth, Guildford, 1984), pp. 457 – 460.
3. J. Knuutila, A.I. Ahonen, M.S. Hämäläinen, R.J. Ilmoniemi, and M.J. Kajola, "Design Considerations for Multichannel SQUID Magnetometers", in: *SQUID'85, Superconducting Quantum Interference Devices and Their Applications*, eds. H.D. Hahlbohm and H. Lübbig. (Walter de Gruyter, Berlin, 1985), pp. 939 – 944.
4. J. Knuutila, S. Ahlfors, A. Ahonen, J. Hällström, M. Kajola, O.V. Lounasmaa, V. Vilkmán, and C. Tesche, "A Large-Area Low-Noise Seven-Channel dc SQUID Magnetometer for Brain Research", Preprint: Report TKK-F-A613. (Helsinki University of Technology, Otaniemi, 1987); *Rev. Sci. Instrum.*, in press (1987).
5. J. Knuutila and M.S. Hämäläinen, "Characterization of Brain Noise Using a High Sensitivity 7-Channel Magnetometer", in: *Proceedings of the Sixth International Conference on Biomagnetism*. (Tokyo Denki University Press, Tokyo, 1987), in press.
6. J. Salmi, J. Knuutila, H. Seppä, and P. Immonen, "Thin Film Process for Nb/NbO<sub>x</sub>/(Pb-In-Au) Josephson Junction Devices", *Thin Solid Films* **126**, 77 – 81 (1985).
7. R. Mutikainen, J. Salmi, and J. Knuutila, "Dependence of the Josephson Tunneling Current on the Normal State Tunneling Resistance for Different Junction Oxidation Methods", in: *Proceedings of the 12th Nordic Semiconductor Meeting*, eds. F. Buschmann, L. Evensen, A. Hanneborg, H. Sandmo, and P. Øhlckers. (Center for Industrial Research, Oslo, 1986), p. 343 – 346.

8. J. Salmi, J. Knuutila, and R. Mutikainen, "In Situ Ion Beam Processing for Josephson Junction Fabrication", in: *Erosion and Growth of Solids Stimulated by Atom and Ion Beams*, eds. G. Kiriakidis, G. Carter, and J.L. Whifton. (Martinus Nijhoff Publishers, Dordrecht, 1986), p. 366 – 369.
9. J. Knuutila, A. Ahonen, and C. Tesche, "Effects on dc SQUID Characteristics of Damping of Input Coil Resonances", *J. Low Temp. Phys.* **68** (3/4), 269 – 284 (1987).
10. J. Knuutila, M. Kajola, H. Seppä, R. Mutikainen, and J. Salmi, "Design, Optimization, and Construction of a dc SQUID with Complete Flux Transformer Circuits", Report **TKK-F-A619**. (Helsinki University of Technology, Otaniemi, 1987).
11. J. Knuutila, M. Kajola, R. Mutikainen, and J. Salmi, "Integrated Planar dc SQUID Magnetometers for Multichannel Neuromagnetic Measurements", in: *Extended Abstracts of the 1987 International Superconductivity Electronics Conference ISEC'87*. (Japan Society of Applied Physics, Tokyo, 1987), p. 261 – 264.

All these publications are results of team work carried out in the Low Temperature Laboratory of Helsinki University of Technology, and in collaboration with the Semiconductor Laboratory and the Electrical Engineering Laboratory of the Technical Research Centre of Finland. After I joined the brain research group in 1981 as an undergraduate student I have participated in the instrument development, which was divided into two simultaneously active main lines. The first part involves the multichannel instrument system design and the construction of few-channel devices, using SQUID components obtained from elsewhere. The second part is concerned with the development of integrated thin film sensors for a new-generation multichannel instrument which, at the time of writing this thesis, is still under construction. The thin-film structures have been fabricated in the Semiconductor Laboratory, and the design, testing, and data analysis has been carried out in the Low Temperature Laboratory.

I have actively taken part in most of the work dealt with in the publications; I had the main responsibility in the preparation of Publications 3, 4, 9, 10, and 11. All the measurements and most of the data analysis of the Josephson junctions described in Publications 6, 7, and 8 were carried out by me as well as the locating error calculations in Paper 1, and the measurements and spectral analysis of the Paper 5.

## 6.2 Summary of Publications

### 1. Analysis of Magnetoencephalographic Data Obtained with a Four-Channel SQUID Magnetometer

Three methods of locating brain activity are compared, based on data obtained with a 4-channel rf SQUID first-order gradiometer and on numerical simulations. The methods include least-squares fitting of a current dipole

to the measured field maps, determination of the equivalent dipole from the maxima of isocontour field maps, and minimum norm estimates for the current distribution. It is concluded that the determination of the dipole location from the field extrema can lead to a large error. If the use of the dipole model is well justified and the spherical model correctly applied, one can approach accuracies on the order of a few millimeters. In addition, an optimal measurement grid spacing is determined for the four-channel magnetometer, and it is noted that significant contribution to the difference between the measured and calculated field values of the equivalent current dipole might come from the variability of the responses between experimental sessions.

## **2. Remarks on the Design of a Four-Channel SQUID Magnetometer for Brain Research**

The design of a 4-channel rf SQUID first order gradiometer, having its pickup coils at the vertices of a regular tetrahedron, is presented. In particular, the rf shielding of the SQUIDs and the mutual interference between the channels are discussed. Design criteria of multichannel magnetometers are presented; for optimization, a formalism based on the lead fields of the sensors is introduced. As an example, the lead field angles, characterizing the amount of independent information of the field sensed by the various channels, are calculated for the 4-channel magnetometer.

## **3. Design Considerations for Multichannel SQUID Magnetometers**

The design criteria for multichannel magnetometers are discussed. In such instruments, the use of planar gradiometers would be beneficial from many practical points of view. The feasibility of using figure-eight shaped first-order off-diagonal planar gradiometers is studied with numerical simulations. As a specific example, a 32-channel device with 24 channels measuring the derivatives of the radial field component and with 8 channels sensing the differences in tangential field components, is considered. Its ability to locate current dipoles in a spherical volume conductor is compared against a 31-channel device having conventional axial first-order gradiometers. Both configurations are shown to yield roughly the same resolution. In addition, practical problems in the use of multichannel magnetometers are discussed, including interchannel interference, calibration of the device, determination of the position and orientation of the magnetometer with respect to the head, and the correlated noise due to the subject.

## **4. A Large-Area Low-Noise Seven-Channel dc SQUID Magnetometer for Brain Research**

The design, construction, and performance of a high-sensitivity dc SQUID magnetometer, covering a circular area of 93 mm in diameter, is described. The device comprises seven asymmetric first-order gradiometers in a hexagonal array, located on a spherical surface of 125 mm radius and tilted 30° with respect to the vertical. The overall sensitivity of the channels is 5 fT/ $\sqrt{\text{Hz}}$ , mainly limited by the thermal noise in the radiation shields. The optimization of the coil configuration and of the measurement system is discussed in



detail. The ability to locate current dipoles is used as a figure-of-merit, and results of simulations with varied coil and measurement array parameters are presented. In addition, the spatial sampling theorem and the lead fields of the channels are considered. Optimization of the dc SQUID performance by eliminating pickup coil resonances is described, and the methods employed to minimize the noise contribution of the electronics system, by matching the output impedance to the preamplifier and by careful shielding and grounding arrangements, are discussed. Finally, an automatic system to determine the position and orientation of the magnetometer with respect to the head is introduced, and some examples of measurements are presented.

## **5. Characterization of Brain Noise Using a High Sensitivity 7-Channel Magnetometer**

The characteristics of spontaneous MEG were studied with the 7-channel magnetometer described in Publication 4. The amplitude spectra and cross-spectra were calculated for the simultaneously measured channels. It was found that the spectrum of the spontaneous background activity extends up to about 50 Hz; below about 20 Hz its level is  $20 - 40 \text{ fT}/\sqrt{\text{Hz}}$ . Coherence analysis showed that this signal is strongly correlated over the area covered by the magnetometer. In evoked response studies, this background activity can often be considered as an extra source of noise. Because of the correlation of this subject noise it is possible to reduce its effect in the analysis. This is demonstrated with an example of a measurement where it is shown that taking the correlation into account reduces the variances of the estimates of equivalent current dipole sources significantly, thus providing more reliable estimates.

## **6. Thin Film Process For Nb/NbO<sub>x</sub>/(Pb-In-Au) Josephson Junction Devices**

A thin-film process for the fabrication of Nb/NbO<sub>x</sub>/(Pb-In-Au) Josephson junctions is described. This process is primarily based on lift-off of the photoresist treated with toluene, ion beam etching of junction areas, dc plasma oxidation, and thin film vacuum deposition techniques. The device characteristics are described in terms of the process parameters.

## **7. Dependence of the Josephson Tunneling Current on the Normal State Tunneling Resistance for Different Junction Oxidation Methods**

The observed critical current density of dc plasma, rf plasma, and ion beam oxidized junctions is compared with the theoretically predicted values, as inferred from the normal-state tunneling resistance. The data are also compared against thermal activation model calculations. For low critical currents damping was found to be very significant. A qualitative agreement of the behavior is found with theoretical predictions for the plasma processes. However, the high noise temperature suggested by the model and the larger deviations for the ion beam processed junctions indicates the existence of other critical current damping mechanisms as well.

## **8. In Situ Ion Beam Processing for Josephson Junction Fabrication**

An ion beam oxidation procedure for fabricating Josephson tunnel junctions is presented, utilizing a mixture of argon and oxygen. The dependence of the critical current density on the ion beam energy is determined; at low ion energies the current density decreases as a function of energy, whereas at higher energies it again rises. This behavior is in agreement with the model of competitive sputter etching by argon and by oxidation. Furthermore, when the critical current density was determined as a function of oxidation time, a steady state, with the resulting current density independent of time, was obtained for long periods of exposure. The spatial variation of the current density showed no systematic variations on the wafer.

## **9. Effects on dc SQUID Characteristics of Damping of Input Coil Resonances**

The possibility of improving the dc SQUID performance by damping the input circuit resonances caused by parasitic capacitances is studied experimentally. A dc SQUID was coupled to a first-order axial gradiometer built for neuromagnetic research, and a resistor-capacitor shunt was connected in parallel with the input coil of the SQUID. Ten different shunts were studied with the SQUID operating in a flux locked loop, carefully shielded against external disturbances. It was found that increasing the shunt resistance resulted in smoother flux-to-voltage characteristics and smaller noise. At best, the minimum obtainable equivalent flux noise level was one-fourth of the unshunted SQUID. The noise level is a function of the shunt resistance  $R_s$  only, except for shunt capacitance values bringing the resonance frequency close to the flux modulating frequency. At a constant bias current level, where the flux-to-voltage response of the SQUID is at maximum, the equivalent flux noise varies as  $R_s^{-0.7}$ . The results agree reasonably well with recently published predictions based on numerical simulations in which the whole input circuit with parasitic capacitances was taken into account.

## **10. Design, Optimization, and Construction of a dc SQUID with Complete Flux Transformer Circuits**

The design of a complete dc SQUID with flux transformer input circuits is discussed. The flux coupling circuits introduce a substantial capacitance across the SQUID and give rise to many resonances which may couple strongly to the SQUID dynamics. Both effects lead to multiple modes in the SQUID and, consequently, to excess noise. For a low-noise SQUID with smooth characteristics, our analysis and practical considerations suggest signal coupling via an intermediary transformer. This allows simultaneous optimization of the SQUID parameters, minimizing the parasitic capacitance, control over the resonances, and good inductance matching to practical magnetometer coils. The elimination of structural resonances is discussed, and a model is developed to optimize the structure. Our analysis describes the whole circuit with the help of a suitably modified autonomous SQUID, provided that the system is free from multiple modes. Following these design principles, a dc SQUID has been built, primarily for use in biomagnetic research but also well

suiting for other applications. The fabrication of the SQUID and the high-quality electronics especially suitable for multi-SQUID devices is presented. The SQUIDs showed smooth characteristics, and the lowest measured noise of the complete SQUID is  $1.3 \times 10^{-6} \Phi_0/\sqrt{\text{Hz}}$ , indicating the success of the design.

#### 11. Integrated Planar dc SQUID Magnetometers for Multichannel Neuromagnetic Measurements

The design, optimization, fabrication, and performance of an all-planar integrated gradiometer is presented. The requirements of low noise and stable operation suggest signal coupling from the pickup coil to the SQUID via an intermediate transformer. This structure allows the field sensing coil and the SQUID to be deposited on separate chips, which has practical advantages. The selected geometry has two orthogonal first-order figure-of-eight gradiometers, with an outer side length of 28 mm, located on a single chip. The dc SQUIDs and the field sensing coils are mounted on a fiber glass support to form a single component. In the design, particular attention is paid to the effects of parasitic elements. Our complete sensors show smooth flux-to-voltage characteristics and a gradient noise smaller than  $450 \text{ fT}/(\text{m} \cdot \sqrt{\text{Hz}})$ , which prove the success of the design and make it a very useful building block for a multichannel magnetometer.

## Acknowledgments

I am indebted to many people for their numerous contributions to this work. First of all, I want to thank Prof. Olli V. Lounasmaa, head of the Low Temperature Laboratory, for his guidance, constructive criticism, encouragement, and support in all phases of preparing this thesis. I have had the privilege of using the outstanding research facilities of the laboratory; the high scientific standard of work carried out in the laboratory has been a constant source of inspiration for me.

Special thanks are due to Dr. Antti Ahonen, leader of the neuromagnetic instrumentation project in 1984 – 1986, for guidance, advice and frictionless collaboration. His desire of doing everything fine and well all the way from beginning has impressed me. Working together with him has really been a pleasure which I will always remember with warmth.

I am obliged to Mr. Jorma Salmi and Mr. Risto Mutikainen from the Semiconductor Laboratory of the Technical Research Centre of Finland for their expertise and diligence in fabricating the thin-film circuits. Their role has been absolutely central and indispensable for the project; this seamless co-operation was started with Jorma Salmi already five years ago. I wish also to express my gratitude to the third key co-worker in developing the SQUID sensors, Mr. Heikki Seppä from the Electrical Engineering Laboratory of the Technical Research Centre for efficient and fruitful collaboration. The numerous discussions on the SQUID design, optimization, and operation have taught me a lot.

Dr. Claudia Tesche from IBM Thomas J. Watson Research Center deserves my warmest thanks for her indispensable co-operation in constructing the seven-channel system by providing her dc SQUIDS at our disposal and by having many stimulating scientific discussions. The work with her has been very pleasant; her visits to the laboratory have always been cheerful occasions.

I am indebted to my near co-workers and friends in the brain research group, Mr. Jari Hällström, Mr. Matti Hämäläinen, Dr. Risto Ilmoniemi, and Mr. Matti Kajola; the close friendship with Matti Hämäläinen, with common musical interests, dates back already before 1981, when we both came in the laboratory as undergraduate students. I have enjoyed their excellent expert collaboration in most aspects dealt with in this thesis; humor and friend's support have created an atmosphere where work really can be fun, even during those late hours many times spent in the laboratory. Also my other co-authors, Mr. Seppo Ahlfors, Mr. Pekka Immonen, Mr. Kalevi Reinikainen, and Mr. Visa Vilkmán all earn my warmest thanks for their fine contributions and pleasant co-operation.

I owe much also to other members of the brain research group. The high-quality neuromagnetic research of Dr. Riitta Hari is one of the main motivating factors for building better instruments. She, Dr. Gösta Ehnholm, and Dr. Jukka Sarvas all deserve my gratitude for their valuable comments, suggestions, and advice. I want also to thank warmly Mr. Arto Annala, Dr. Juha Huttunen, Ms. Sirkka-Liisa

Joutsiniemi, Mr. Ari Järvi, Ms. Pia Kemppainen, Mr. Mikko Kiviranta, Dr. Lea Leinonen, Mr. Jyrki Mäkelä, Dr. Elina Pihko, Mr. Willi Plöger, Mr. Jyrki Saarinen, and Ms. Satu Tissari for their help, pleasant colleagueship and friendship. It has been a privilege to work in this group; also, many joyful moments in the leisure with friends from the group, often in concerts or recitals, shall stay in my mind forever.

Dr. Sergei Chabanov, Mr. Istvan Derka, and Dr. Heinrich Seifert are thanked for their contributions to the SQUID electronics, Mr. Tapani Ryhänen for his valuable simulations of the SQUID dynamics in collaboration with Heikki Seppä, and Dr. Alexandr Inyushkin for his work in packaging the integrated gradiometer. I am also grateful to Mr. Heikki Ahola, Prof. Gordon Donaldson, Dr. William Gallagher, Dr. Konstantin Gurtovoy, Dr. David Hutson, Dr. Pekka Karp, Dr. Alan Kleinsasser, Dr. Hannes Nowak, Dr. Colin Pegrum, Dr. Marco Pelizzone, Dr. Auvo Penttinen, Dr. Stanley Raider, Mr. Robert Sandstrom, Dr. Ilkka Suni, Dr. Wolfgang Vodel, and Dr. Viktor Vvedensky for fruitful discussions and comments.

The staff of the Low Temperature Laboratory is thanked for all help during this work. Especially I want to devote my warmest thanks to Ms. Marja Holmström for her indispensable help and tremendously flexible attitude in making the laboratory research run smoothly, well equipped and provided with all necessary accessories. I wish also to thank Mr. Seppo Kaivola, Mr. Antti Huvila, Mr. Juhani Kaasinen, and Mr. Hannu Kaukelin from the laboratory workshop and Mr. Arvi Isomäki and Mr. Antero Salminen from the cryocenter for their skillful technical assistance. Mr. Jukka Koponen is thanked for his valuable help in preparing the figures and Mr. Mauri Laakso from the University of Helsinki for his photographic services. I owe also much to the laboratory staff for providing a pleasant and stimulating atmosphere to work in.

The neuromagnetic instrumentation project has been supported financially by SITRA, TEKES, the Academy of Finland, Kone Corp., Nokia Corp., and Instrumentarium Corp. A personal grant from Jenny and Antti Wihuri Foundation as well as conference travel grants from the Cultural Foundation of Finland and Magnus Ehrnrooth Foundation are gratefully acknowledged.

Last but not least, I wish to express my sincere and deepest gratitude to my dear parents and brother for their continuous encouragement and support in all phases of the work, making my efforts easier.

Helsinki, October 27, 1987



Jukka Knuutila

## References

- [1] R. Hari and R.J. Ilmoniemi, "Cerebral Magnetic Fields", *CRC Crit. Rev. in Biomed. Engin.* **14** (2), 93 (1986).
- [2] S.W. Kuffler, J.G. Nicholls, and A.R. Martin, *From Neuron to Brain*, 2nd Edition. (Sinauer Associates, Sunderland, 1984).
- [3] D.B. Geselowitz, "On the Magnetic Field Generated Outside an Inhomogeneous Volume Conductor by Internal Current Sources", *IEEE Trans. Magn.* **MAG-6** (2), 346 (1970).
- [4] D.B. Geselowitz, "On Bioelectric Potentials in an Inhomogeneous Volume Conductor", *Biophys. J.* **7** (7), 1 (1967).
- [5] J. Sarvas, "Basic Mathematical and Electromagnetic Concepts of the Biomagnetic Inverse Problem", *Phys. Med. Biol.* **32** (1), 11 (1987).
- [6] M.S. Hämäläinen and J. Sarvas, *Realistic Conductivity Geometry Model of the Human Head for Interpretation of Neuromagnetic Data*, Report TKK-F-A614. (Helsinki University of Technology, Otaniemi, 1987).
- [7] M.S. Hämäläinen, H. Haario, and M.S. Lehtinen, *Inferences about Sources of Neuromagnetic Fields using Bayesian Parameter Estimation*, Report TKK-F-A620. (Helsinki University of Technology, Otaniemi, 1987).
- [8] H.W. Sorenson, *Parameter Estimation: Principles and Problems*. (Marcel Dekker, New York, 1980).
- [9] R. Hari, S.-L. Joutsiniemi, and J. Sarvas, "Spatial Resolution of Neuromagnetic Recordings: Theoretical Calculations in a Spherical Model", *Electroenceph. Clin. Neurophysiol.*, in press (1987).
- [10] J. Knuutila, A.I. Ahonen, M.S. Hämäläinen, R.J. Ilmoniemi, and M.J. Kajola, "Design Considerations for Multichannel SQUID Magnetometers", in: *SQUID'85, Superconducting Quantum Interference Devices and Their Applications*, eds. H.D. Hahlbohm and H. Lübbig. (Walter de Gruyter, Berlin, 1985), p. 939.
- [11] R. Hari, M. Pelizzone, J.P. Mäkelä, J. Hällström, L. Leinonen, and O.V. Lounasmaa, "Neuromagnetic Responses of the Human Auditory Cortex to On- and Offsets of Noise Bursts", *Audiology* **26**, 31 (1987).
- [12] J. Huttunen, R. Hari, and L. Leinonen, "Cerebral Magnetic Responses to Stimulation of Ulnar and Median Nerves", *Electroenceph. Clin. Neurophysiol.* **66** (4), 391 (1987).
- [13] E. Kaukoranta, R. Hari, M. Hämäläinen, and J. Huttunen, "Cerebral Magnetic Fields Evoked by Peroneal Nerve Stimulation", *Somatosensory Research* **3** (4), 309 (1986).
- [14] F. London, *Superfluids*, Vol 1. (Wiley, New York, 1950).

- [15] B.D. Josephson, "Possible New Effects in Superconductive Tunnelling", *Phys. Lett.* **1** (7), 251 (1962).
- [16] K.K. Likharev, "Superconducting Weak Links", *Rev. Mod. Phys.* **51** (1), 101 (1979).
- [17] A. Barone and G. Paterno, *Physics and Applications of the Josephson Effect* (Wiley, New York, 1982).
- [18] W.C. Stewart, "Current-Voltage Characteristics of Josephson junctions", *Appl. Phys. Lett.* **12** (8), 277 (1968).
- [19] D.E. McCumber, "Effect of ac Impedance on dc Voltage-Current Characteristics of Superconductor Weak-Link Junctions", *J. Appl. Phys.* **39** (7), 3113 (1968).
- [20] D.E. McCumber, "Tunneling and Weak-Link Superconductor Phenomena Having Potential Device Applications", *J. Appl. Phys.* **39** (6), 2503 (1968).
- [21] V. Ambegaokar and A. Baratoff, "Tunneling between Superconductors", *Phys. Rev. Lett.* **10** (11), 486 (1963). Erratum: **11** (2), 104 (1963).
- [22] R.F. Broom, S.I. Raider, A. Oosenbrug, R.E. Drake, and W. Walter, "Niobium Oxide-Barrier Tunnel Junction", *IEEE Trans. Electron Dev.* **ED-27** (10), 1998 (1980).
- [23] W.J. Gallagher, S.I. Raider, and R.E. Drake, "Electrical Characterization of Nb/Nb Oxide/PbAuIn Josephson Tunnel Junctions", *IEEE Trans. Magn.* **MAG-19** (3), 807 (1983).
- [24] J.H. Magerlein, "Specific Capacitance of Josephson Tunnel Junctions", *IEEE Trans. Magn.* **MAG-17** (1), 286 (1981).
- [25] L. Young, *Anodic Oxide Films*. (Academic Press, New York, 1971).
- [26] J.C. Villegier and G. Matheron, "Some Properties of Nb<sub>2</sub>O<sub>5</sub> Thermally Grown Tunnel Barriers in Nb-Nb<sub>2</sub>O<sub>5</sub>-Pb(In) Josephson Junctions", in: *SQUID'85, Superconducting Quantum Interference Devices and Their Applications*, eds. H.D. Hahlbohm and H. Lübbig. (Walter de Gruyter, Berlin, 1985), p. 381.
- [27] B.D. Josephson, "Coupled Superconductors", *Rev. Mod. Phys.* **36**, 216 (1964).
- [28] N. Uchida, K. Enpuku, Y. Matsugaki, S. Tomita, and F. Irie, "Flux Trapping in Josephson Tunnel Junctions", *J. Appl. Phys.* **54** (9), 5287 (1983).
- [29] T.A. Fulton and L.N. Dunkleberger, "Lifetime of the Zero-Voltage State in Josephson Tunnel Junctions", *Phys. Rev. B* **9** (11), 4760 (1974).
- [30] A. Barone, R. Cristiano, and P. Silvestrini, "Supercurrent Decay in Underdamped Josephson Junctions: Nonstationary Case", *J. Appl. Phys.* **58** (10), 3822 (1985).
- [31] S.I. Raider, "Josephson Tunnel Junctions with Refractory Electrodes", *IEEE Trans. Magn.* **MAG-21** (2), 110 (1985).
- [32] A.I. Braginski, "Recent Advances in Josephson Junction Materials", in: *Extended Abstracts of the 1987 International Superconductivity Electronics Conference ISEC'87*. (Japan Society of Applied Physics, Tokyo, 1987), p. 63.
- [33] S.A. Reible, "Reactive Ion Etching in the Fabrication of Niobium Tunnel Junctions", *IEEE Trans. Magn.* **MAG-17** (1), 303 (1981).

- [34] R.E. Lee, "Microfabrication by Ion-Beam Etching", *J. Vac. Sci. Technol.* **16** (2), 164 (1979).
- [35] M. Gurvitch, M.A. Washington, and H.A. Huggins, "High Quality Refractory Josephson Tunnel Junctions Utilizing Thin Aluminum Layers", *Appl. Phys. Lett.* **42** (5), 472 (1983).
- [36] A. Shoji, S. Kosaka, F. Shinoki, M. Ayoagi, and H. Hayakawa, "All Refractory Josephson Tunnel Junctions Fabricated by Reactive Ion Etching", *IEEE Trans. Magn.* **MAG-19** (3), 827 (1983).
- [37] S. Morohashi, S. Hasuo, and T. Yamaoka, "Self-Aligned Contact Process for Nb/Al-AlO<sub>x</sub> Josephson Junctions", *Appl. Phys. Lett.* **48** (3), 254 (1986).
- [38] A.K. Jain, J.E. Sauvageau, D.B. Schwartz, K.T. Springer, and J.E. Lukens, "Fabrication of Niobium-Lead Tunnel Junctions Using a Self Aligned Masking Technique", *IEEE Trans. Magn.* **MAG-21** (2), 955 (1985).
- [39] T. Imamura, H. Hoko, and S. Hasuo, "Integration Process for Josephson LSI Based on Nb/AlO<sub>x</sub>/Nb Junctions", in: *Extended Abstracts of the 1987 International Superconductivity Electronics Conference ISEC'87*. (Japan Society of Applied Physics, Tokyo, 1987), p. 57.
- [40] R.F. Broom, A. Oosenbrug, and W. Walter, "Josephson Junctions of Small Area Formed on the Edges of Niobium Films", *Appl. Phys. Lett.* **37** (2), 237 (1980).
- [41] A.W. Kleinsasser and R.A. Buhrman, "High-Quality Submicron Niobium Tunnel Junctions with Reactive-Ion-Beam Oxidation", *Appl. Phys. Lett.* **37** (9), 841 (1980).
- [42] H. Koch, "Self-Aligned In-Line Junction — Fabrication and Application in dc SQUIDS", in: *Extended Abstracts of the 1987 International Superconductivity Electronics Conference ISEC'87*. (Japan Society of Applied Physics, Tokyo, 1987), p. 281.
- [43] J.H. Greiner, "Josephson Tunneling Barriers by rf Sputter Etching in an Oxygen Plasma", *J. Appl. Phys.* **42** (12), 5151 (1971).
- [44] W. Schroen, "Physics of Preparation of Josephson Barriers", *J. Appl. Phys.* **39** (6), 2671 (1968).
- [45] J. Salmi, J. Knuutila, H. Seppä, and P. Immonen, "Thin Film Process For Nb/NbO<sub>x</sub>/(Pb-In-Au) Josephson Junction Devices", *Thin Solid Films* **126**, 77 (1985).
- [46] S.I. Raider and R.E. Drake, "Nb/Nb Oxide/Pb-Alloy Josephson Tunnel Junctions", *IEEE Trans. Magn.* **MAG-17** (1), 299 (1981).
- [47] S.I. Raider, R.W. Johnson, T.S. Kuan, R.E. Drake, and R.A. Pollak, "Characterization of Nb/Nb Oxide Structures in Josephson Tunnel Junctions", *IEEE Trans. Magn.* **MAG-19** (3), 803 (1983).
- [48] T.S. Kuan, S.I. Raider, and R.E. Drake, "Structure of a Nb Oxide Tunnel Barrier in a Josephson Junction", *J. Appl. Phys.* **53** (11), 7464 (1982).
- [49] A.W. Kleinsasser, "Relationship between Beam and Junction Parameters in Ion Beam Processed Josephson Devices", *J. Appl. Phys.* **57** (7), 2575 (1985).
- [50] S.S. Pei and R.B. van Dover, "Ion Beam Oxidation for Josephson Circuit Applications", *Appl. Phys. Lett.* **44** (7), 703 (1984).



- [51] A.H. Silver and J.E. Zimmerman, "Quantum States and Transitions in Weakly Connected Superconducting Rings", *Phys. Rev.* **157** (2), 317 (1967).
- [52] J. Clarke, "Advances in SQUID Magnetometers", *IEEE Trans. Electron Dev.* **ED-27** (10), 1896 (1980).
- [53] O.V. Lounasmaa, *Experimental Principles and Methods Below 1 K*. (Academic Press, New York, 1974).
- [54] J. Kurkijärvi, "Intrinsic Fluctuations in a Superconducting Ring Closed with a Josephson Junction", *Phys. Rev. B* **6** (3), 832 (1972).
- [55] J. Kurkijärvi and W.W. Webb, "Thermal Fluctuation Noise in a Superconducting Flux Detector", *Proceedings of the 1972 Applied Superconductivity Conference*. (IEEE, New York, 1972), p. 581.
- [56] J. Kurkijärvi, "Noise in the Superconducting Quantum Flux Detector", *J. Appl. Phys.* **44** (8), 3729 (1973).
- [57] L.D. Jackel and R.A. Buhrman, "Noise in the rf SQUID", *J. Low Temp. Phys.* **19** (3/4), 201 (1975).
- [58] J. Kurkijärvi, "Collective Quantum Tunneling, Ultimate Sensitivity of the ac SQUID, and All That", *J. Low Temp. Phys.* **45** (1/2), 37 (1981).
- [59] G.J. Ehnholm, "Theory of the Signal Transfer and Noise Properties of the rf SQUID", *J. Low Temp. Phys.* **29** (1/2), 1 (1977).
- [60] R.C. Jaklevic, J. Lambe, J.E. Mercereau, and A.H. Silver, "Macroscopic Quantum Interference in Superconductors", *Phys. Rev.* **140** (5A), A1628 (1965).
- [61] J.E. Zimmerman and A.H. Silver, "Macroscopic Quantum Interference Effects through Superconducting Point Contacts", *Phys. Rev.* **141** (1), 367 (1966).
- [62] J. Clarke, W.M. Goubau, and M.B. Ketchen, "Tunnel Junction dc SQUID: Fabrication, Operation, and Performance", *J. Low Temp. Phys.* **25** (1/2), 99 (1976).
- [63] R.F. Voss, R.B. Laibowitz, A.N. Broers, S.I. Raider, C.M. Knoedler, and J.M. Viggiano, "Ultra Low Noise Nb dc SQUIDS", *IEEE Trans. Magn.* **MAG-17** (1), 395 (1981).
- [64] M.W. Cromar and P. Carelli, "Low-Noise Tunnel Junction dc SQUID's", *Appl. Phys. Lett.* **38** (9), 723 (1981).
- [65] D.J. Van Harlingen, R.H. Koch, and J. Clarke, "Superconducting Quantum Interference Device with Very Low Magnetic Flux Noise Energy", *Appl. Phys. Lett.* **41** (2), 197 (1982).
- [66] M.B. Ketchen, "dc SQUIDS 1980: The State of the Art", *IEEE Trans. Magn.* **MAG-17** (1), 387 (1981).
- [67] J. Clarke, "Ultrasensitive Measuring Devices", *Physica* **126B** (1-3), 441 (1984).
- [68] C.D. Tesche and J. Clarke, "dc SQUID: Noise and Optimization", *J. Low Temp. Phys.* **29** (3/4), 301 (1977).
- [69] V.J. de Waal, P. Schrijner, and R. Llurba, "Simulation and Optimization of a dc SQUID with Finite Capacitance", *J. Low Temp. Phys.* **54** (3/4), 215 (1984).

- [70] J.J.P. Bruines, V.J. de Waal, and J.E. Mooij, "Comment on: 'dc SQUID: Noise and Optimization' by Tesche and Clarke", *J. Low Temp. Phys.* **46** (3/4), 383 (1982).
- [71] E. Ben-Jacob and Y. Imry, "Dynamics of the dc SQUID", *J. Appl. Phys.* **52** (11), 6806 (1981).
- [72] E. Ben-Jacob, D.J. Bergman, Y. Imry, B.J. Matkowsky, and Z. Schuss, "Thermal Activation from the Fluxoid and the Voltage States of dc SQUIDS", *J. Appl. Phys.* **54** (11), 6533 (1983).
- [73] J.A. Ketoja, J. Kurkijärvi, and R.K. Ritala, "Instabilities and Chaotic Solutions of the Current Biased dc Superconducting Quantum Interference Device", *Phys. Rev. B* **30** (7) 3757 (1984).
- [74] J.A. Ketoja, J. Kurkijärvi, T. Ryhänen, and H. Seppä, "Reply to 'Noise Effect on Instabilities and Chaotic Solutions of a Superconducting Interferometer'", *Phys. Rev. B*, **35** (1), 404 (1987).
- [75] R.W. Henry, D.E. Prober, "Electronic Analogs of Double-Junction and Single-Junction SQUIDS", *Rev. Sci. Instrum.* **52** (6), 902 (1981).
- [76] C.D. Tesche, "A Thermal Activation Model for Noise in the dc SQUID", *J. Low Temp. Phys.* **44** (1/2), 119 (1981).
- [77] C.D. Tesche, "Analysis of a Double-Loop dc SQUID", *J. Low Temp. Phys.* **47** (5/6), 385 (1982).
- [78] R.H. Koch, J. Clarke, W.M. Goubau, J.M. Martinis, C.M. Pegrum, and D.J. Van Harlingen, "Flicker ( $1/f$ ) Noise in Tunnel Junction dc SQUIDS", *J. Low Temp. Phys.* **51** (1/2), 207 (1983).
- [79] J. Clarke and G. Hawkins, "Flicker ( $1/f$ ) Noise in Josephson Tunnel Junctions", *Phys. Rev. B* **14** (7), 2826 (1976).
- [80] C.T. Rogers and R.A. Buhrman, "Composition of  $1/f$  Noise in Metal-Insulator-Metal Tunnel Junctions", *Phys. Rev. Lett.* **53** (13), 1272 (1984).
- [81] R.T. Wakai and D.J. van Harlingen, "Low-Frequency Noise and Discrete Charge Trapping in Small-Area Tunnel Junction dc SQUID's", *Appl. Phys. Lett.* **49** (10), 593 (1986).
- [82] H. Seppä, T. Ryhänen, and J. Kurkijärvi, "Thermal Feedback Model of  $1/f$  Noise in Josephson Junctions", submitted to *Phys. Rev. B*.
- [83] C.D. Tesche, K.H. Brown, A.C. Callegari, M.M. Chen, J.H. Greiner, H.C. Jones, M.B. Ketchen, K.K. Kim, A.W. Kleinsasser, H.A. Notarys, G. Proto, R.H. Wang, and T. Yogi, "Practical dc SQUIDS with Extremely Low  $1/f$  Noise", *IEEE Trans. Magn.* **MAG-21** (2), 1032 (1985).
- [84] V. Foglietti, W.J. Gallagher, M.B. Ketchen, A.W. Kleinsasser, R.H. Koch, S.I. Raider, and R.L. Sandstrom, "Low-Frequency Noise in Low  $1/f$  Noise dc SQUID's", *Appl. Phys. Lett.* **49** (20), 1393 (1986).
- [85] J.E. Zimmerman, "Sensitivity Enhancement of Superconducting Quantum Interference Devices through the Use of Fractional-Turn Loops", *J. Appl. Phys.* **42** (11), 4483 (1971).
- [86] J.M. Jaycox and M.B. Ketchen, "Planar Coupling Scheme for Ultra Low Noise dc SQUIDS", *IEEE Trans. Magn.* **MAG-17** (1), 400 (1981).

- [87] P. Carelli and V. Foglietti, "Behavior of a Multiloop dc Superconducting Quantum Interference Device", *J. Appl. Phys.* **53** (11), 7592 (1982).
- [88] P. Carelli and V. Foglietti, "Improved Multi-Loop dc SQUID", *IEEE Trans. Magn.* **MAG-19** (3), 299 (1983).
- [89] B. Muhlfelder, W. Johnson, and M.W. Cromar, "Double Transformer Coupling to a Very Low Noise SQUID", *IEEE Trans. Magn.* **MAG-19** (3), 303 (1983).
- [90] B. Muhlfelder, J.A. Beall, M.W. Cromar, R.H. Ono, and W.W. Johnson, "Well Coupled, Low Noise, dc SQUIDS", *IEEE Trans. Magn.* **MAG-21** (2), 427 (1985).
- [91] B. Muhlfelder, J.A. Beall, M.W. Cromar, and R.H. Ono, "Very Low Noise, Tightly Coupled, dc SQUID Amplifiers", *Appl. Phys. Lett.* **49** (17), 1118 (1986).
- [92] K. Enpuku, K. Sueoka, K. Yoshida, and F. Irie, "Effect of Damping Resistance on Voltage versus Flux Relation of a dc SQUID with Large Inductance and Critical Current", *J. Appl. Phys.* **57** (5), 1691 (1985).
- [93] K. Enpuku, T. Muta, K. Yoshida, and F. Irie, "Noise Characteristics of a dc SQUID with a Resistively Shunted Inductance", *J. Appl. Phys.* **58** (5), 1916 (1985).
- [94] K. Enpuku and K. Yoshida, "Resistively Shunted dc SQUID Coupled to an Input Coil", *J. Appl. Phys.* **59** (5), 1714 (1986).
- [95] K. Enpuku, K. Yoshida, and S. Kohjiro, "Noise Characteristics of a dc SQUID with a Resistively Shunted Inductance. II. Optimum Damping", *J. Appl. Phys.* **60** (12), 4218 (1986).
- [96] N. Ohkawa, T. Noguchi, and N. Tsukada, "Measurements of Noise Characteristics of a dc SQUID with a Resistively Shunted Inductance", *Japan. J. Appl. Phys.* **26** (Supplement 26-3), 1643 (1987).
- [97] M.B. Ketchen, W.M. Goubau, J. Clarke, and G.B. Donaldson, "Superconducting Thin-Film Gradiometer", *J. Appl. Phys.* **49** (7), 4111 (1978).
- [98] V.J. de Waal and T.M. Klapwijk, "Compact Integrated dc SQUID Gradiometer", *Appl. Phys. Lett.* **41** (7), 669 (1982).
- [99] V.J. de Waal, T.M. Klapwijk, and P. van den Hamer, "High Performance dc SQUIDS with Submicrometer Josephson Junctions", *J. Low Temp. Phys.* **53** (3/4), 287 (1983).
- [100] V.J. de Waal, G.J. van Nieuwenhuyzen, and T.M. Klapwijk, "Design and Performance of Integrated dc SQUID Gradiometers", *IEEE Trans. Magn.* **MAG-19** (3), 648 (1983).
- [101] P. Carelli and V. Foglietti, "A Second Derivative Gradiometer Integrated with a dc Superconducting Interferometer", *J. Appl. Phys.* **54** (10), 6065 (1983).
- [102] G.J. van Nieuwenhuyzen and V.J. de Waal, "Second Order Gradiometer and dc SQUID Integrated on a Planar Surface", *Appl. Phys. Lett.* **46** (4), 439 (1985).
- [103] G.B. Donaldson, C.M. Pegrum, and R.J.P. Bain, "Integrated Thin Film SQUID Instruments", in: *SQUID'85, Superconducting Quantum Interference Devices and Their Applications*, eds. H.D. Hahlbohm and H. Lübbig. (Walter de Gruyter, Berlin, 1985), p. 729.

- [104] M.B. Ketchen, "Integrated Thin-Film dc SQUID Sensors", *IEEE Trans. Magn.* **MAG-23** (2), 1650 (1987).
- [105] M.B. Ketchen, "Design of Improved Integrated Thin-Film Planar dc SQUID Gradiometers", *J. Appl. Phys.* **58** (11), 4322 (1985).
- [106] F. Wellstood, C. Heiden, and J. Clarke, "Integrated dc SQUID Magnetometer with a High Slew Rate", *Rev. Sci. Instrum.* **55** (6), 952 (1984).
- [107] M. Nakanishi, M. Koyanagi, S. Kosaka, A. Shoji, M. Ayoagi, F. Shinoki, H. Nakagawa, S. Takada, N. Kasai, H. Kado, and T. Endo, "Integrated dc SQUID Magnetometer", in: *Extended Abstracts of the 1987 International Superconductivity Electronics Conference ISEC'87*. (Japan Society of Applied Physics, Tokyo, 1987), p. 265.
- [108] D. Drung, E. Crocoll, R. Herwig, A. Knüttel, M. Neuhaus, and W. Jutzi, "Experimental Gradiometer with a Digital Feedback Loop", in: *Extended Abstracts of the 1987 International Superconductivity Electronics Conference ISEC'87*. (Japan Society of Applied Physics, Tokyo, 1987), p. 21.
- [109] M. Gershenson, R. Hastings, R. Schneider, M. Sweeny, and E. Sorensen, "SQUID Linear Amplifier Circuit Simulations", *IEEE Trans. Magn.* **MAG-19** (5), 2058 (1983).
- [110] D. Drung and W. Jutzi, "Hysteretic Noise Simulation of dc SQUIDS with Input Coil", in: *SQUID'85, Superconducting Quantum Interference Devices and Their Applications*, eds. H.D. Hahlbohm and H. Lübbig. (Walter de Gruyter, Berlin, 1985), p. 807.
- [111] H. Seppä and T. Ryhänen, "Influence of the Signal Coil on dc SQUID Dynamics", *IEEE Trans. Magn.* **MAG-23** (2), 1083 (1987).
- [112] C. Hilbert and J. Clarke, "Measurements of the Dynamic Input Impedance of a dc SQUID", *J. Low Temp. Phys.* **61** (3/4), 237 (1985).
- [113] P. Carelli and V. Foglietti, "Problems in Coupling a dc SQUID to the External World", *IEEE Trans. Magn.* **MAG-21** (2), 424 (1985).
- [114] R.S. Germain, M.L. Roukes, M.R. Freeman, R.C. Richardson, and M.B. Ketchen, "Source Impedance Effects on dc SQUID Performance", *Proceedings of the 17th International Conference on Low Temperature Physics LT-17*, eds. U. Eckern, A. Schmid, W. Weber, and H. Wühl. (Elsevier, Amsterdam, 1984), p. 203.
- [115] C.D. Tesche, "Analysis of Strong Inductive Coupling on SQUID Systems", *IEEE Trans. Magn.* **MAG-19** (3), 458 (1983).
- [116] J.M. Martinis and J. Clarke, "Signal and Noise Theory for a dc SQUID Amplifier", *J. Low Temp. Phys.* **61** (3/4), 227 (1985).
- [117] C.M. Pegrum, D. Hutson, G.B. Donaldson, and A. Tugwell, "dc SQUIDS with Planar Input Coils", *IEEE Trans. Magn.* **MAG-21** (2), 1036 (1985).
- [118] R.J. Ilmoniemi, R. Hari, and K. Reinikainen, "A Four-Channel SQUID Magnetometer for Brain Research", *Electroenceph. Clin. Neurophysiol.* **58** (5), 467 (1984).
- [119] G.J. Murphy, *Control Engineering*. (D. van Nostrand Company, Princeton, 1959).

- [120] R.P. Giffard, "Fundamentals for SQUID Applications", in: *SQUID'80, Superconducting Quantum Interference Devices and Their Applications*, eds. H.D. Hahlbohm and H. Lübbig, (Walter de Gruyter, Berlin, 1980), p. 445.
- [121] Y. Netzer, "A New Interpretation of Noise Reduction by Matching", *Proc. IEEE* **62** (3), 404 (1974).
- [122] Y. Netzer, "The Design of Low-Noise Amplifiers", *Proc. IEEE* **69** (6), 728 (1981).
- [123] G.L. Romani, S.J. Williamson, and L. Kaufman, "Biomagnetic Instrumentation", *Rev. Sci. Instrum.* **53** (12), 1815 (1982).
- [124] D. Duret and P. Karp, "Instrumentation for Biomagnetism", *Il Nuovo Cimento* **2D** (2), 123 (1983).
- [125] D.E. Farrell and P. Zanzucchi, "SQUID Biomagnetic Measurements", *CRC Crit. Rev. in Solid State and Mater. Sci.* **11** (2), 99 (1983).
- [126] J. Vrba, A.A. Fife, M.B. Burbank, H. Weinberg, and P.A. Brickett, "Spatial Discrimination in SQUID Gradiometers and 3rd order Gradiometer Performance", *Can. J. Phys* **60**, 1060 (1982).
- [127] D. Duret and P. Karp, "Figure of Merit and Spatial Resolution of Superconducting Flux Transformers", *J. Appl. Phys.* **56** (6), 1762 (1984).
- [128] D. Cohen, "Magnetic Measurement and Display of Current Generators in the Brain. Part I: The 2-D Detector", in: *Proceedings of the 12th International Conference on Medical and Biological Engineering*. (Jerusalem, 1979), p. 15.
- [129] S.J. Williamson, M. Pelizzzone, Y. Okada, L. Kaufman, D.B. Crum, and J.R. Marsden, "Five Channel SQUID Installation for Unshielded Neuromagnetic Measurements", in: *Biomagnetism: Applications & Theory*, eds. H. Weinberg, G. Stroink, and T. Katila. (Pergamon Press, New York, 1985), p. 46.
- [130] G.L. Romani, R. Leoni, C. Salustri, "Multichannel Instrumentation for Biomagnetism", in: *SQUID'85, Superconducting Quantum Interference Devices and Their Applications*, eds. H.D. Hahlbohm and H. Lübbig. (Walter de Gruyter, Berlin, 1985), p. 919.
- [131] Biomagnetic Technologies, Inc., 4174 Sorrento Valley Blvd., San Diego, California 92121, USA
- [132] K. Shirae, H. Furukawa, and K. Kishida, "A New Multi-Element rf SQUID System and its Application to the Magnetic Vector Gradiometer", *Cryogenics* **21** (12), 707 (1981).
- [133] M. Seppänen, T. Katila, T. Tuomisto, T. Varpula, D. Duret, and P. Karp, "Measurement of Biomagnetic Fields Using Multichannel Superconducting-Magnetometer Techniques", *Il Nuovo Cimento* **2D** (2), 166 (1983).
- [134] J.O. Lekkala and J.A.V. Malmivuo, "Multiplexed SQUID Vectormagnetometer for Biomagnetic Research", *J. Phys. E: Sci. Instrum.* **17** (6), 504 (1984).
- [135] S.N. Ern , G.L. Romani, "Performances of Higher Order Planar Gradiometers for Biomagnetic Source Localization", in: *SQUID'85, Superconducting Quantum Interference Devices and Their Applications*, eds. H.D. Hahlbohm and H. Lübbig. (Walter de Gruyter, Berlin, 1985), p. 951.
- [136] P. Carelli and R. Leoni, "Localization of Biological Sources with Arrays of Superconducting Gradiometers", *J. Appl. Phys.* **59** (2), 645 (1986).

- [137] G.L. Romani and R. Leoni, "Localization of Cerebral Sources by Neuromagnetic Measurements", in: *Biomagnetism: Applications & Theory*, eds. H. Weinberg, G. Stroink, and T. Katila. (Pergamon Press, New York, 1985), p. 205.
- [138] H.J.M. ter Brake, F.H. Fleuren, J.A. Ulfman, and J. Flokstra, "Elimination of Flux-Transformer Crosstalk in Multichannel SQUID Magnetometers", *Cryogenics* **26** (12), 667 (1986).
- [139] M. Pelizzone, R. Hari, J.P. Mäkelä, J. Huttunen, S. Ahlfors, and M. Hämäläinen, "Cortical Origin of Middle-Latency Auditory Evoked Responses in Man", *Neurosci. Lett.*, in press (1987).
- [140] R.M. Chapman, R.J. Ilmoniemi, S. Barbanera, and G.L. Romani, "Selective Localization of Alpha Brain Activity with Neuromagnetic Measurements", *Electroenceph. Clin. Neurophysiol.* **58** (6), 569 (1984).
- [141] J.G. Bednorz and K.A. Müller, "Possible High  $T_c$  Superconductivity in the Ba-La-Cu-O System", *Z. Phys. B* **64** (2), 189 (1986).
- [142] M.K. Wu, J.R. Ashburn, C.J. Torng, P.H. Hor, R.L. Meng, L. Gao, Z.J. Huang, Y.Q. Wang, C.W. Chu, "Superconductivity at 93 K in a New Mixed-Phase Y-Ba-Cu-O Compound System at Ambient Pressure", *Phys. Rev. Lett.* **58** (9), 908 (1987).
- [143] *Proceedings of the 18th International Conference on Low Temperature Physics*, Vols. 1 – 2: *Japan. J. Appl. Phys.* **26** (Supplement 26-3) (1987), Vol. 3: *Japan. J. Appl. Phys.*, in press (1987).
- [144] D. Estève, J.M. Martinis, C. Urbina, M.H. Devoret, G. Collin, P. Monod, M. Ribault, and A. Revcolevschi, "Observation of the ac Josephson Effect Inside Copper-Oxide-Based Superconductors", *Europhysics Letters* **3** (11), 1237 (1987).
- [145] A. Inoue, K. Takeuchi, H. Ito, A. Nakayama, Y. Okabe, "Y-Ba-Cu-O/Au/ $\text{AlO}_x$ /Nb Josephson Junctions", in: *Extended Abstracts of the 1987 International Superconductivity Electronics Conference ISEC'87*. (Japan Society of Applied Physics, Tokyo, 1987), p. 413.
- [146] Y. Higashino, T. Takahashi, T. Kawai, and S. Naito, "Observation of the Josephson Effect in Y-Ba-Cu-O Compound", *Japan. J. Appl. Phys.* **26** (7), L1211 (1987).
- [147] H. Tanabe, S. Kita, and T. Kobayashi, "ac Josephson Effect in Point-Contact (Y,Er)BaCuO Ceramics and Films", in: *Extended Abstracts of the 1987 International Superconductivity Electronics Conference ISEC'87*. (Japan Society of Applied Physics, Tokyo, 1987), p. 397.
- [148] P.H. Wu, Q.H. Cheng, S.Z. Yang, J. Chen, Y. Li, Z.M. Ji, and J.M. Song, "The Josephson Effect in Ceramic Bridge at Liquid Nitrogen Temperature", in: *Extended Abstracts of the 1987 International Superconductivity Electronics Conference ISEC'87*. (Japan Society of Applied Physics, Tokyo, 1987), p. 392.
- [149] R.H. Koch, C.P. Umbach, G.J. Clark, P. Chaudhari, and R.B. Laibowitz, "Quantum Interference Devices Made from Superconducting Oxide Thin Films", *Appl. Phys. Lett.* **51** (3), 200 (1987).
- [150] H. Nakane, T. Nishino, M. Hirano, K. Takagi, and U. Kawabe, "dc SQUID Using High-Critical-Temperature Oxide-Superconductors", in: *Extended Ab-*

- stracts of the 1987 International Superconductivity Electronics Conference ISEC'87.* (Japan Society of Applied Physics, Tokyo, 1987), p. 411.
- [151] I. Iguchi, A. Sugishita, and M. Yanagisawa, "dc SQUID Operation at 77 K Using All Ceramics Josephson Junctions", *Japan. J. Appl. Phys.* **26** (6), L1021 (1987).
  - [152] J.E. Zimmerman, J.A. Beall, M.W. Cromar, R.H. Ono, "Operation of a Y-Ba-Cu-O rf SQUID at 81 K", *Appl. Phys. Lett.* **51** (8), 617 (1987).
  - [153] G.B. Donaldson, "From 4.2 K to 77 K in Six Months — Superconductive Electronics in Europe", in: *Extended Abstracts of the 1987 International Superconductivity Electronics Conference ISEC'87.* (Japan Society of Applied Physics, Tokyo, 1987), p. 10.
  - [154] R. Laiho, K. Naukkarinen, and J. Vanhatalo, unpublished (1987).
  - [155] R.M. Chapman, G.L. Romani, S. Barbanera, R. Leoni, I. Modena, G.B. Ricci, and F. Campitelli, "SQUID Instrumentation and the Relative Covariance Method for Magnetic 3D Localization of Pathological Cerebral Sources", *Il Nuovo Cimento* **38**, 549 (1983).
  - [156] D.S. Barth, W. Sutherling, J. Engel, Jr., and J. Beatty, "Neuromagnetic Evidence of Spatially Distributed Sources Underlying Epileptiform Spikes in the Human Brain", *Science* **223**, 293 (1984).

